ATOMISTIC SIMULATIONS OF MAGNETIC SHAPE MEMORY ALLOYS

Jussi Enkovaara

Laboratory of Physics
Helsinki University of Technology

Fysiikan laboratorio
Teknillinen korkeakoulu

DISSERTATION 119 (2003)

ATOMISTIC SIMULATIONS OF MAGNETIC SHAPE MEMORY ALLOYS

Jussi Enkovaara

Laboratory of Physics
Helsinki University of Technology
Espoo, Finland

Dissertation for the degree of Doctor of Science in Technology to be presented with due permission of the Department of Engineering Physics and Mathematics, Helsinki University of Technology for public examination and debate in Auditorium E at Helsinki University of Technology (Espoo, Finland) on the 21st of February, 2003, at 12 o'clock noon.

Dissertations of Laboratory of Physics, Helsinki University of Technology
ISSN 1455-1802

Dissertation 119 (2003):
Jussi Enkovaara: Atomistic Simulations of Magnetic Shape Memory Alloys
ISBN 951-22-6313-0 (print)
ISBN 951-22-6319-X (electronic)

OTAMEDIA OY
ESPOO 2003

Kulkurille, missä kuljetkaan...

Abstract

Magnetic shape memory (MSM) alloys are novel smart materials which exhibit magnetic field induced strains of up to 10 %. As such they have potential for many technological applications. Also, the strong magneto-structural couplings of the MSM effect make the phenomenon very interesting from a scientific point of view. In this thesis, materials and properties related to the MSM effect are studied with atomistic simulations. Main interest is in the known MSM alloy Ni-Mn-Ga around the Ni_2MnGa stoichiometry.

One pre-requisite for the MSM effect is the existence of a structural transformation in a magnetic material, and therefore some candidate materials are investigated from this perpective. Here, Ni_2MnAl is found to have potential for further studies. The magnetic moment is seen to originate mainly from Mn in the Mn-containing alloys and the existence of different structural phases is ascribed to a band Jahn-Teller effect in the Ni band. This picture is confirmed by comparisons between theoretical and experimental neutron diffraction results. In Ni_2MnGa the structural phase transformations are found to be driven by vibrational entropy at finite temperatures.

The magnetic key property in the MSM effect is the magnetic anisotropy energy which is studied in Ni_2MnGa. The tetragonal structure with $c/a = 0.94$ is magnetically uniaxial characterized by the first anisotropy constant, but in the presence of several twin variants only the second anisotropy constant may be observed in the measurements. Analysis of the microscopic origins of the magnetic anisotropy shows that Ni has the largest contribution to the magnetic anisotropy energy. Investigations of other structures show that in Ni_2MnGa the shortest crystal axis is always the easy axis of magnetization. From other magnetic properties, the Curie temperatures of Ni_2MnGa and Ni_2MnAl are estimated on the basis of total energy calculations of spin spirals. Ni is found to have an important effect also on the Curie temperatures despite its smaller magnetic moment when compared to Mn.

Non-stoichiometric compositions of Ni-Mn-Ga are studied within the rigid band approximation and with supercell calculations. In some cases the rigid band approximation describes the correct trends, but more insight into the alloying effects can be obtained from the supercell calculations. The most important result of these investigations is that in Mn-rich compositions the extra Mn atoms couple antiferromagnetically to the neighbouring Mn

atoms. This result implies a decrease of the total magnetic moment with Mn-doping. Also, all the experimentally observed martensite phases are explained theoretically when the extra Mn is explicitly included.

Preface

I had my first touch with the magnetic shape memory alloys already during my first summer assignment in the Laboratory of Physics, so when starting this thesis project in 1999 I already had some idea about the subject. However, I did not know about all the interesting physics connected with these intriguing materials. I have learned a lot during the course where the supervision of Dr. Andrés Ayuela has been crucial. He has helped and encouraged me in many things also outside the field of physics. He has always had time for student and working (and especially traveling) with him has never been boring. I consider myself lucky as I have had the opportunity to work in a very competitive theoretical group and I am grateful to professor Risto Nieminen for that. He has allowed the student to concentrate on research without need to worry about financial issues. As theoretician it is important to be in touch also with the real world and I want to thank all the people in the MSM-project for interesting discussions. Dr. Lars Nordström guided me in the calculations of magnetic anisotropy and non-collinear magnetism and provided also his programs for my use. The working atmosphere in the Laboratory of Physics has been excellent and I want to thank the whole personnel for their contribution to that. Especially I want to thank Dr. Erkki Hellén who shared the room with me for almost six years.

Haluan kiittää kaikkia ystäviäni, sekä erityisesti sisartani ja vanhempiani jotka ovat rohkaisseet minua opiskeluissani. Vaimoni Johanna on rakastanut minua ja ollut tukenani myös vaikeina hetkinä. Hän on jaksanut myös kärsivällisesti kuunnella selityksiäni fysiikasta. Lopuksi haluan kiittää lapsiani Eetua ja Iidaa jotka ovat kiitettävästi onnistuneet viemään ajatukseni työstä tärkeämpiin asioihin.

Espoo, February 2003

Jussi Enkovaara

Contents

List of publications

This thesis consists of an overview and the following publications:

I. A. Ayuela, J. Enkovaara, K. Ullakko, and R. M. Nieminen, *Structural properties of magnetic Heusler alloys*, J. Phys.:Condens. Matter **11**, 2017-2026 (1999)

II. A. Ayuela, J. Enkovaara, and R. M. Nieminen, *Ab-initio study of tetragonal variants in Ni_2MnGa alloy*, J. Phys.:Condens. Matter **14**, 5325-5336 (2002)

III. J. Enkovaara, A. Ayuela, L. Nordström, and R. M. Nieminen, *Structural, thermal and magnetic properties of Ni_2MnGa*, J. Appl. Phys. **91**, 7798-7800 (2002)

IV. J. Enkovaara, A. Ayuela, L. Nordström, and R. M. Nieminen, *Magnetic anisotropy in Ni_2MnGa*, Phys. Rev. B **65**, 134422 (2002) (*6 pages*)

V. J. Enkovaara, A. Ayuela, J. Jalkanen, L. Nordström, and R. M. Nieminen, *First principles calculations of spin spirals in Ni_2MnGa and Ni_2MnAl*, accepted for publication in Phys. Rev. B

VI. J. Enkovaara, O. Heczko, A. Ayuela, and R. M. Nieminen, *Coexistence of ferro- and antiferromagnetic order in Mn-doped Ni_2MnGa*, submitted for publication in Phys. Rev. Lett.

The author has had an active role in all phases of the research reported in this thesis. He has been involved in the planning of the calculations, in the development of the computer programs, and in the interpretation of the results. The author has had the main responsiblity of the writing of Publications III-VI and he has contributed actively to the writing and publication process of all the papers. He has performed all the calculations in Publications III and IV, and most of the calculations in the other Publications.

1 Introduction

The development of active materials is attaining increasing interest in the the materials science community [1]. These are materials which respond intrinsically to external impulses, for example in the form of shape changes. Magnetic shape memory (MSM) alloys [2] are a novel class of these kind of materials which can function both as actuators and as sensors. The MSM alloys show shape changes of several percent upon application of an external magnetic field. This effect has potential for many technological applications, for example in robotics and active noise control.

The structural properties, such as the equilibrium crystal structures and elastic constants, are important for all materials. Some materials may undergo structural phase transformations and show superelastic stress responses and shape memory effects. On the other hand, magnetic materials are characterized by spontaneous magnetic moments whose ordering can affect for example the electrical conductivity. Usually, the magnetic moments respond to the external magnetic fields without significant structural changes. The interesting feature in the MSM effect is the strong coupling between structural and magnetic degrees of freedom. As such, magnetic shape memory alloys provide a fascinating playground for basic research with interesting physical problems without losing their solid link to the applications.

Developments in computer technology have allowed the investigations of realistic systems with fully *ab initio* approach, *i.e.* simulations starting from the basic quantum mechanics with only the atomic numbers of the constituent elements as the input parameters. These kind of simulations can offer information which is difficult to obtain experimentally, for example about the effects of the underlying electronic structure on the material properties. The calculations can be also helpful in suggesting new experiments. Because of their predictive power a certain subclass of given candidate materials or compositions can be outlined theoretically without the need for time consuming and expensive experiments.

In this thesis atomic scale *ab initio* simulations are used to study materials and properties related to the magnetic shape memory effect. The present view of the mechanism of the MSM effect is presented in the end of this Section. The research is focused mainly on the known MSM alloy Ni-Mn-Ga, and some of its experimentally known properties are reviewed

in Sec. 2. The computational framework used in this thesis is outlined in Sec. 3. The investigations include a wide range of structural, thermal and magnetic properties in stoichiometric compounds as well as in some non-stoichiometric compounds as presented in Sec. 4. Finally, the conclusions are given in Sec. 5.

1.1 Magnetic shape memory effect

The phenomenon of magnetostriction where an external magnetic field can change the dimensions of the sample was observed already in 1842 by Joule. In normal ferromagnets such as Fe or Ni the strains associated with the magnetostriction are of the order of 10^{-4}% while materials with exceptionally large magnetostriction, for example Tb-Dy-Fe alloys (Terfenol-D), show strains of the order of 0.1% [3]. In contrast, MSM materials can show magnetic field induced strains of 10% [4]. Not only are the strains in the MSM effect two orders of magnitude larger, but also the mechanism is different from ordinary magnetostriction. While ordinary magnetostriction is observed in structurally homogeneous samples, the MSM effect requires a special microstructure. This microstructure is provided by a martensitic transformation. The martensitic transformation [5, 6] is a displacive,diffusion free structural transformation from a higher symmetry structure (austenite) to a lower symmetry structure (martensite) upon cooling. For example, in Ni_2MnGa the high symmetry phase is cubic while the lower symmetry phase can be tetragonal or orthorhombic. In order to minimize the total shape change (and the macroscopic strain energy) over the whole sample, some microstructure develops in the martensitic phase. A common way to create this kind of microstructure is twinning: because there are usually several crystallographically equivalent ways to deform the high symmetry structure, the deformation may take different directions in different regions of the sample. These structural domains have well defined boundaries and they are called twin variants. A schematic example of the twinning is seen in Fig. 1.

Twin boundaries are often mobile which is exploited in the temperature driven shape memory effect [7]. Due to the easy movement of the twin boundaries the sample can be deformed easily in the martensitic phase. When the material is heated back to the austenitic phase the sample will revert to its original shape, *i.e.* it will "remember" the shape it had before cooling. Even though strains in the temperature-driven shape memory effect

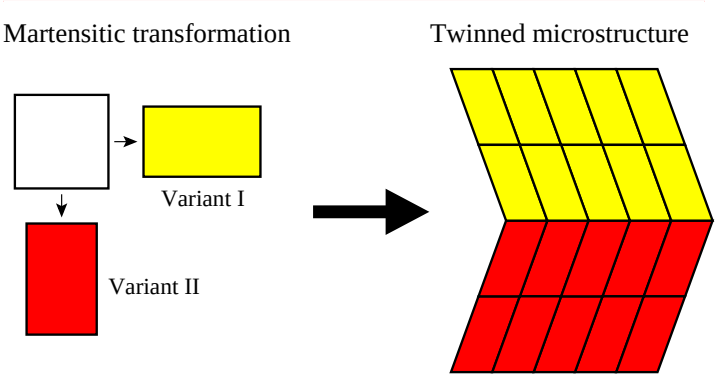

Figure 1: Schematic illustration of the martensitic transformation and twinning in two dimensions.

can be several percent, the heating and especially the cooling are relatively slow processes. Therefore a way to drive the shape change with a faster response would be desirable for many applications. This can be achieved by taking the magnetic degrees of freedom into play.

Magnetic materials such as ferromagnets, antiferromagnets and ferrimagnets are characterized by spontaneous magnetic moments. Also, in the absence of an external magnetic field their magnetization has a certain preferable direction with respect to the crystal lattice, the so-called easy direction. In a twinned microstructure the lattice orientations of the twin variants are different and therefore the magnetization directions also differ, as shown in Fig. 2a. When an external magnetic field is applied, the magnetic moments try to align with the field. If the energy needed to rotate the magnetization away from the easy direction, the magnetic anisotropy energy, is high enough, it may be energetically favourable to move the twin boundaries instead. The fraction of twins where the easy axis is in the direction of the field will grow at the expense of the other twin variants. This process results in large shape changes as shown schematically in Fig. 2b.

Based on the above discussion the basic requirements for the appearance of the MSM effect can be summarized:

- The material should be (ferro)magnetic and exhibit martensitic transformation.
- The magnetic anisotropy energy should be higher than the energy needed to move the twin boundaries.

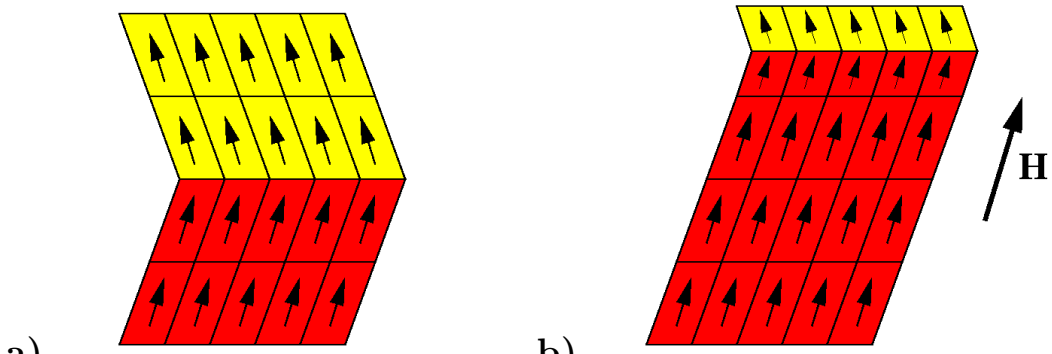

Figure 2: a) Magnetic moments without the external field. b) Redistribution of the variants in an applied field.

From the point of view of practical applications the material should be in the martensitic phase at room temperature. The strength of the required external field depends on the local magnetic moment of the material, so the magnetic moment should be high.

At the moment, the MSM effect has been observed in Fe-Pd [8], Co-Ni-Ga [9], La-Sr-CuO_4 [10] and Ni-Mn-Ga [2, 4, 11] alloys. La-Sr-CuO_4 is interesting as it is not a ferromagnet but an antiferromagnet, confirming that the magnetic anisotropy is more important than the macroscopic magnetic moment. For practical applications the most promising material is Ni-Mn-Ga. As most of the work in this thesis concerns Ni-Mn-Ga some of its experimentally known properties are reviewed next.

2 Experimental studies of Ni-Mn-Ga

Numerous studies of Ni-Mn-Ga alloys have appeared in recent years. Here, a brief summary of the experimental results is given, concentrating on the properties which will be discussed from the theoretical point of view later on.

At the martensitic phase transformation, energy is released or absorbed, and this can be measured by differential scanning calorimetry (DSC). Also, the response to the external magnetic field changes at the transition, allowing the phase transformations to be observed in magnetic susceptibility measurements. These methods allow detection of the occurrence of the transformation and determination of the corresponding temperatures. The advantage of the magnetic susceptibility is that the Curie temperature is also observed clearly as the susceptibility changes abruptly in the ferromagnetic to paramagnetic transition. On the other hand, DSC measurements allow the energetics of the transition to be studied. Some examples of these measurement are shown in Fig. 3.

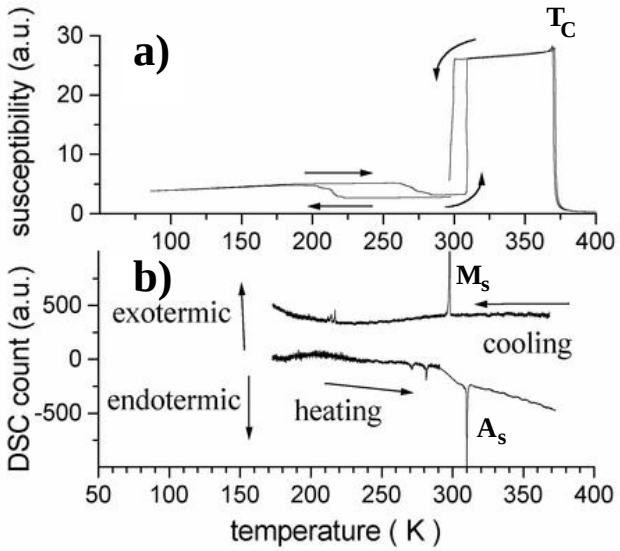

Figure 3: Examples of a) magnetic susceptibility and b) differential calorimetry, showing the martensitic and austenitic transformation temperatures M_s and A_s and the Curie temperature T_C. Courtesy of O. Heczko.

The martensitic transformation temperatures span over a wide range, from 160 K to 620 K [12–16] and they vary strongly with composition as a $\sim$1% change in the composition can alter the transformation temperature by 50 degrees. In addition to the austenite-martensite transformation, up to two intermartensitic transformations can be observed. The Curie temperature is less sensitive to the composition and it is between 320 K and 380 K [16–18].

The crystal structures of the different phases can be studied with X-ray and neutron diffraction. The high temperature austenitic phase has the cubic $L2_1$ structure which is shown in Fig. 4, with a lattice constant $a_{L2_1} = 11.01$ a.u. [17, 19]. This structure has the f.c.c. Bravais lattice with a four atom basis. As the constituent atoms have similar atomic numbers it can be difficult to distinguish them from the X-ray data. In this case the structure can be interpreted as a b.c.c. structure with a lattice constant half from that of the f.c.c. lattice.

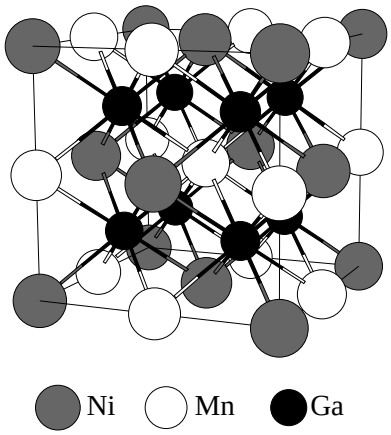

Figure 4: Cubic $L2_1$ structure with atomic positions of the stoichiometric composition.

Three different martensite structures are observed. Two of them have a basic tetragonal symmetry and one has an orthorhombic symmetry. In the first tetragonal structure the ratio of the c and the a lattice constants is $c/a \sim 0.94$ [17]. In addition, there is a shuffling of the atomic planes. The $(1\bar{1}0)$ planes show a modulation in the [110] direction with a period of 5 atomic planes and the structure can be designated as 5M [13, 20]. The other tetragonal structure has the deformation $c/a \gtrsim 1.2$ and it can be denoted as non-modulated (NM) because there is no modulation of the atomic planes

[13, 21, 22]. The orthorhombic structure has the lattice constant ratios $b/a = 0.94$ and $c/a = 0.89$ and it is designated as 7M since it has a 7 layer modulation similar to the other tetragonal structure [4, 13, 23, 24]. The volume remains approximately constant during all the transformations.

The first martensite which appears on cooling depends on the composition, but the stability of the structures *i.e.* the order in which they appear on cooling seems to be always the same. This is shown schematically in Fig. 5a. The NM structure is the most stable before the 7M structure [13, 21, 25]. If the 5M structure is to be observed it is transformed directly from the austenite. There is also an empirical correlation between the austenite-martensite transformation temperatures and the first martensite structure as shown in Fig. 5b [15, 26]. The alloys transforming directly to the NM structure typically have transformation temperatures which can be higher than the Curie point [27, 28] and the 7M phase appears first only in a narrow temperature range [4, 26, 29].

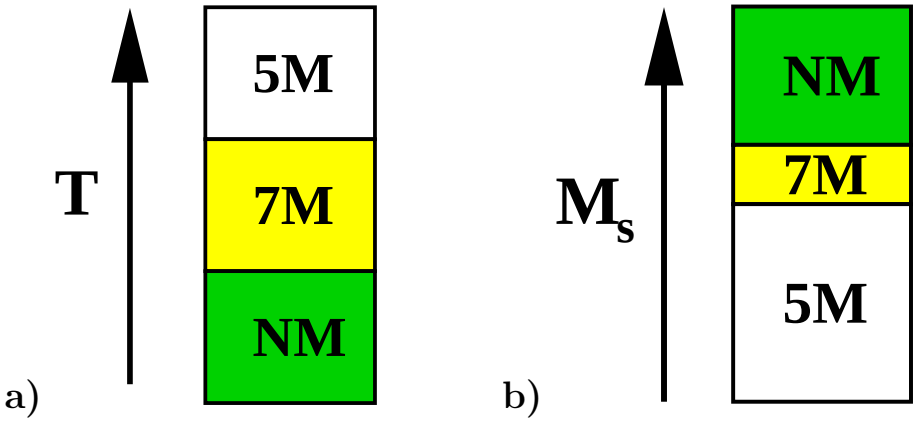

Figure 5: a) The stability of the martensitic phases. b) Relation between the first martensite structure and the transformation temperature M_s.

The lattice constant ratios give the maximum strain which is available from the twin rearrangement. This limit is 6% in the 5M structure, 10% in the 7M structure, and over 20% in the NM structure. Up to now, the maximum strain has been realized as magnetic-field-induced both in the 5M [11, 30] and in the 7M structures [4]. In the NM structure the MSM effect has not been observed.

As neutrons possess a magnetic moment, neutron diffraction provides information also about the local magnetic moments. The total magnetic moment in the stoichiometric composition is found to be 4.1 μ_B per formula unit and it originates mainly from Mn [17, 19, 31]. Another experimental method for the determination of the saturation magnetization is the vibrating sample magnetometer (VSM). VSM measurements do not reveal individual atomic magnetic moments, but on the other hand it is possible to obtain the magnetic anisotropy energy. With VSM one measures the magnetization as a function of the external field, as shown in Fig. 6. By applying this field in different directions with respect to the crystal axis the magnetic anisotropy energy can be determined as the area between the two magnetization curves. The magnetic anisotropy energy and the easy axis depend on the particular martensite. In the 5M the [001] direction (the short c-axis) is the easy axis and the magnetic anisotropy energy is around 2.0×10^5 J/m^3 at room temperature [30, 32, 33]. In the non-modulated tetragonal structure [001] is the hard direction and there is an easy plane with an anisotropy energy of 3.0×10^5 J/m^3 [21, 34]. In the orthorhombic 7M structure there are three inequivalent directions. The shortest axis has the lowest energy, the longest axis the highest energy and the energy of the intermediate axis is in-between. The largest energy difference is about 2.2×10^5 J/m^3 [4, 34].

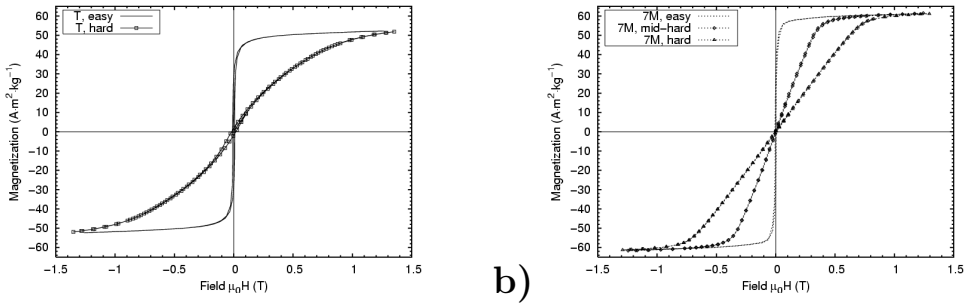

Figure 6: Magnetization as a function of the external magnetic field with different field directions in a) the NM (T in the figure) structure and b) the 7M structure. Courtesy of L. Straka.

In the following sections the above discussed properties are studied from a theoretical point of view, in some cases also for other materials than Ni-Mn-Ga. It will be seen that the calculations can predict and explain with simple arguments much of the experimentally observed behaviour.

3 The many-body problem

The determination of the properties of solid state systems from basic quantum mechanics is desirable. The wave function Ψ contains all the information about the system. In principle, it can be obtained by solving the Schrödinger equation

$$H\Psi = E\Psi, \tag{1}$$

where H is the Hamiltonian operator and E is the total energy of the N-particle system. However, the wave function depends on the coordinates and the spins of all the particles so that Ψ is a function of $4N$ variables. As the number of particles in condensed matter systems is of the order of 10^{23}, an exact solution of Eq. (1) is not possible. Therefore some approximations have to be introduced in order to solve the many-body problem.

First, the Born-Oppenheimer approximation decouples the nuclear and electronic degrees of freedom. The nuclei are several orders of magnitude heavier than the electrons, so electrons respond quickly to the motions of the nuclei. Therefore the nuclei can be considered as an external potential for the electronic subsystem and the electronic part is solved as a function of the nuclear positions. Even though the Schrödinger equation is solved only for the electrons, the number of particles is still too large in most cases and one has to introduce further approximations.

There are basically two different approaches to the problem. In the first one, some approximate wave function is constructed, as for example in the Hartree and the Hartree-Fock approximations. These methods express the full many-body wave function $\Psi(\boldsymbol{r}_1, \boldsymbol{r}_2, ..., \boldsymbol{r}_n)$ in terms of single-particle wave functions $\psi(\boldsymbol{r}_1), \psi(\boldsymbol{r}_2), ..., \psi(\boldsymbol{r}_n)$. In the Hartree approximation [35] a product of the single-particle wave functions is used which leads to N single-particle equations. However, this many-body wave function does not obey the Pauli exclusion principle which makes the theoretical foundation of the Hartree approximation unsound. The Hartree-Fock approach [36, 37] fulfills the Pauli exclusion principle by expressing the many-body wave function as a Slater determinant of the single-particle wave functions. However, the ensuing equations are much more difficult to solve than the corresponding Hartree equations, while important physics is still missing from the Hartree-Fock approximation. Wave functions beyond the Hartree-Fock approximation can be constructed for example as a series of Slater determinants but the computational burden increases very rapidly so that only very small systems can be studied.

An alternative approach to the many-body problem was initiated by Thomas [38] and Fermi [39] who formulated the problem in terms of the electron density instead of the wave function. Since the density is a function of three space coordinates only, the number of degrees of freedom is reduced drastically. The ideas of the Thomas-Fermi approximation are elaborated in the density-functional theory which is discussed next.

3.1 Density-functional theory

The density-functional theory provides an exact formulation of the many-body problem in terms of the particle density. It is based on two theorems by Hohenberg and Kohn [40]:

- For a given external potential, the ground state energy is a unique functional of the electron density.
- The minimum of the energy functional is obtained with the ground state density.

These theorems imply that all the ground state properties can be calculated on the basis of the density alone.

When studying magnetic properties it is convenient to work both with the electron density and the magnetization density. The density matrix $\underline{\boldsymbol{\rho}}$ is defined as

$$\underline{\boldsymbol{\rho}}(\boldsymbol{r}) = [n(\boldsymbol{r})\underline{\mathbf{1}} + \boldsymbol{m}(\boldsymbol{r}) \cdot \underline{\boldsymbol{\sigma}}]/2, \tag{2}$$

where $n(\boldsymbol{r})$ is the electron density, $\underline{\mathbf{1}}$ is a 2x2 identity matrix, $\boldsymbol{m}(\boldsymbol{r})$ is the magnetization density and $\underline{\boldsymbol{\sigma}}$ is a vector of the Pauli spin matrices. Following the arguments of Hohenberg and Kohn it can be shown that the ground state energy is a functional of the density matrix [41]. The energy functional can be separated as

$$E[\underline{\boldsymbol{\rho}}(\boldsymbol{r})] = T[\underline{\boldsymbol{\rho}}(\boldsymbol{r})] + W[\underline{\boldsymbol{\rho}}(\boldsymbol{r})] + U[\underline{\boldsymbol{\rho}}(\boldsymbol{r})], \tag{3}$$

where T is the kinetic energy of the many-electron system, W is the electron-electron interaction energy and U is the interaction energy due to an external potential $v_{ext}(\boldsymbol{r})$ and a magnetic field $\boldsymbol{b}_{ext}(\boldsymbol{r})$. If the form of the functional were known, its minimization with respect to the density matrix

would give the ground state energy as well as the ground state density and magnetization.

As an alternative to direct minimization, the problem can be mapped into an equivalent set of single particle equations [42]. First, the functional $F = T + W$ is divided into

$$F[\underline{\boldsymbol{\rho}}(\boldsymbol{r})] = T_0[n(\boldsymbol{r})] + E_C[n(\boldsymbol{r})] + E_{xc}[\underline{\boldsymbol{\rho}}(\boldsymbol{r})], \tag{4}$$

where T_0 is the kinetic energy of *non-interacting* electrons with the density $n(\boldsymbol{r})$ and magnetization $\boldsymbol{m}(\boldsymbol{r})$, and E_C is the classical Coulomb energy of the electrons. The last term E_{xc} contains all the remaining many-body effects and is called the exchange-correlation energy. The idea is that T_0 and E_C, which are known exactly, give the largest contributions to F, while the unknown part E_{xc} should be smaller.

Next, one introduces single-particle spinors ψ_i

$$\psi_i = \begin{pmatrix} \phi_i^{\uparrow} \\ \phi_i^{\downarrow} \end{pmatrix}, \tag{5}$$

where $\phi^{\uparrow}$ and $\phi^{\downarrow}$ are the spin-up and the spin-down components of the spinor. With the help of these spinors the energy functional Eq. (3) can be written as

$$\begin{aligned} E = &\sum_i \langle \psi_i | \hat{T}_0 | \psi_i \rangle + \iint \frac{n(\boldsymbol{r}) n(\boldsymbol{r'})}{|\boldsymbol{r} - \boldsymbol{r'}|} d\boldsymbol{r} d\boldsymbol{r'} + E_{xc}[\underline{\boldsymbol{\rho}}(\boldsymbol{r})] \\ &+ \int (v_{ext}(\boldsymbol{r}) n(\boldsymbol{r}) + \boldsymbol{b}_{ext}(\boldsymbol{r}) \cdot \boldsymbol{m}(\boldsymbol{r})) d\boldsymbol{r}, \end{aligned} \tag{6}$$

where $\hat{T}_0$ is the kinetic energy operator. The density and magnetization of the *interacting* electrons are obtained from the two component spinors

$$\begin{aligned} n(\boldsymbol{r}) &= \sum_i \langle \psi_i | \psi_i \rangle \\ \boldsymbol{m}(\boldsymbol{r}) &= \sum_i \langle \psi_i | \underline{\boldsymbol{\sigma}} | \psi_i \rangle. \end{aligned} \tag{7}$$

The summations are over the occupied states so that the integration of the charge density produces the correct number of electrons N_e in the system, $\int n(\boldsymbol{r}) d\boldsymbol{r} = N_e$. Variational minimization of the energy functional of Eq. (6) results in

$$(\hat{T}_0 + \underline{\boldsymbol{V}}_{eff}) \psi_i = e_i \psi_i \tag{8}$$

with an effective potential matrix

$$\underline{\boldsymbol{V}}_{eff}(\boldsymbol{r}) = \left(\int \frac{n(\boldsymbol{r}')}{|\boldsymbol{r} - \boldsymbol{r}'|} d\boldsymbol{r}' + v_{ext}(\boldsymbol{r}) \right) \underline{\mathbf{1}} + \boldsymbol{b}_{ext}(\boldsymbol{r}) \cdot \underline{\boldsymbol{\sigma}} + \frac{\delta E_{xc}[\underline{\boldsymbol{\rho}}(\boldsymbol{r})]}{\delta \underline{\boldsymbol{\rho}}(\boldsymbol{r})}. \quad (9)$$

The complicated many-body problem is therefore mapped into an equivalent set of single-particle equations which are easy to solve as soon as the effective potential is known.

Because the effective potential depends on the density matrix, the equations have to be solved in an iterative way. One constructs first a guess for the density matrix. After solving ψ_i from the single particle equation Eq. (8), a new density matrix and an effective potential are constructed from Eqs. (7) and (9). The procedure is continued until self-consistency is reached, *i.e.* the input and output densities are the same.

The functional derivative of the exchange-correlation energy, the exchange-correlation potential, can be separated into electric and magnetic parts as

$$\frac{\delta E_{xc}[\underline{\boldsymbol{\rho}}(\boldsymbol{r})]}{\delta \underline{\boldsymbol{\rho}}(\boldsymbol{r})} = v_{xc}(\boldsymbol{r}) \underline{\mathbf{1}} + \boldsymbol{b}_{xc}(\boldsymbol{r}) \cdot \underline{\boldsymbol{\sigma}}, \quad (10)$$

where the scalar part v_{xc} results from the functional derivation with respect to density and the vector part $\boldsymbol{b}_{xc}$ from the derivation with respect to the magnetization. The whole effective potential matrix can be now separated for electric and magnetic parts,

$$\underline{\boldsymbol{V}}_{eff} = v_{eff} \underline{\mathbf{1}} + \boldsymbol{b}_{eff} \cdot \underline{\boldsymbol{\sigma}}. \quad (11)$$

Relativistic effects can be included by using the relativistic kinetic energy operator of the Dirac equation

$$\underline{\boldsymbol{\alpha}} \cdot \hat{\boldsymbol{p}} + \beta \quad (12)$$

in the single particle equation Eq. (8) (For the definitions of $\underline{\boldsymbol{\alpha}}$ and β see for example Ref. [43]). Usually, a fully relativistic treatment is not necessary and it is enough to include the leading order terms in v/c . These terms can be divided into the so-called scalar relativistic corrections [44] and into the spin-orbit coupling [45]

$$\xi(r) \boldsymbol{l} \cdot \underline{\boldsymbol{\sigma}} = -\frac{1}{r} \frac{dv_{eff}}{dr} \boldsymbol{l} \cdot \underline{\boldsymbol{\sigma}}, \quad (13)$$

where $\boldsymbol{l}$ is the orbital angular momentum. By omitting the scalar relativistic corrections, the Kohn-Sham equation Eq. (8) can be finally written as

$$\left(\left(-\nabla^2/2 + v_{eff}\right)\underline{\mathbf{1}} + \boldsymbol{b}_{eff}\cdot\underline{\boldsymbol{\sigma}} + \xi(r)\boldsymbol{l}\cdot\underline{\boldsymbol{\sigma}}\right)\psi_i = e_i\psi_i. \tag{14}$$

Some notes can be made about the structure of Eq. (14). In a non-magnetic case the effective potential is a scalar times the identity matrix and Eq. (14) reduces to a scalar equation. Also, in the case where the spin-orbit coupling can be neglected and there is a global spin quantization axis, the Hamiltonian in Eq. (14) diagonalises in spin. The spinors have a pure spin up or down character and one can solve two scalar equations with a spin-dependent scalar potential. However, in a general case when the spin-orbit coupling is included or in the absence of a global spin quantization axis the full matrix equation has to be solved. In this case the spin is not a good quantum number, and the spinors will have a mixed spin-up and down characters.

3.1.1 Approximations for the exchange-correlation functional

Up to now, the mapping of the many-body problem into a set of single particle equations has been exact. However, the exchange-correlation energy has to be approximated in some way. A common description is provided by the local spin density approximation (LSDA) [41]. The basic assumption is that *locally* the electron gas can be considered as homogeneous so that the exchange-correlation energy can be written as

$$E_{xc} = \int n(\boldsymbol{r})e_{xc}(n(\boldsymbol{r}), m(\boldsymbol{r}))d\boldsymbol{r}, \tag{15}$$

where $e_{xc}(n, m)$ is the exchange-correlation energy density of the homogeneous electron gas with density n and magnetization magnitude m. As the magnetization dependence of the exchange-correlation energy is through the magnitude of the magnetization, the magnetic part of the exchange-correlation potential is collinear with the magnetization density *i.e.* $\boldsymbol{b}_{xc} \times \boldsymbol{m} = 0$.

Although the LSDA was formulated for slowly varying densities it works well in many cases where this assumption should in fact not be valid. For example, calculated lattice constants and magnetic moments in solid-state systems are within few percent of the experimental values. One well-known

shortcoming of the LSDA is its incorrect description of the ground state structure of Fe. There, an improvement is provided by the generalized gradient approximation (GGA) [46, 47]. It takes into account also the gradients of the density and the magnetization as

$$E_{xc} = \int f(n(\boldsymbol{r}), m(\boldsymbol{r}), \nabla n(\boldsymbol{r}), \nabla m(\boldsymbol{r}))d\boldsymbol{r}. \tag{16}$$

While the LSDA has a tendency for overbinding, the GGA usually overcorrects the LSDA by underbinding. There are, however, problems where neither LSDA or GGA give the correct results. These include the band gaps in the semiconductors and insulators, and ground states of systems with strong electron-electron correlations. Also, in the calculation of magnetic anisotropy of fcc Ni both approximations result in the wrong easy axis.

3.2 Computational methods

3.2.1 Brillouin zone integrations

The translational invariance of a crystal leads to the Bloch theorem: each electronic state can be characterized by a wave vector $\boldsymbol{k}$ in the first Brillouin zone [48],

$$\psi_{\boldsymbol{k}}(\boldsymbol{r}) = e^{i\boldsymbol{k}\cdot\boldsymbol{r}} u_{\boldsymbol{k}}(\boldsymbol{r}). \tag{17}$$

In order to obtain the kinetic energy, the charge density and the magnetization density, summations such as in Eq. (7) have to be carried over the Brillouin zone. For an infinite periodic crystal this requires in principle an infinite number of $\boldsymbol{k}$-points. In practice one can of course use only finite numbers of $\boldsymbol{k}$-points and different schemes have been developed in order to obtain accurate results with a minimum number of points.

Taking into account the symmetry of the crystal it is possible to construct a set of special $\boldsymbol{k}$-points in the Brillouin zone and calculate the integrals as weighted summations [49]. In the case of insulators and semiconductors the energy bands are continuous as there are no states at the Fermi-level and the direct summation gives accurate results with a small number of $\boldsymbol{k}$-points. In metals the occupied energy bands are discontinuous at the Fermi level, and the direct summation converges slowly with the number

of $\boldsymbol{k}$-points. A better convergence is obtained with broadening methods [50, 51] or with the tetrahedron method [52, 53]. The broadening methods treat the discontinous bands by averaging over the Fermi-level, while the tetrahedron method uses an interpolation which allows the integrals to be evaluted analytically.

3.2.2 Full-potential linearized augmented plane wave method

The Kohn-Sham equations provide a convenient formalism for the solution of the many-body problem. Still, some specific numerical method is needed in order to solve the equations. One possibility is to solve the differential equations directly on a numerical mesh [54]. Here, another approach is used where a set of basis functions is used in reformulating the differential equations into matrix equations.

In principle, any function can be presented as a linear combination of a complete set of functions. The Kohn-Sham orbitals are expanded as

$$\psi = \sum c_G \phi_G, \tag{18}$$

where we drop out the index i. With the help of the basis functions ϕ_G the Kohn-Sham equations can be formulated as a generalized eigenvalue problem

$$\underline{\boldsymbol{H}}\boldsymbol{c} = e\underline{\boldsymbol{S}}\boldsymbol{c}, \tag{19}$$

where $H_{G,G'} = \langle \phi_G | H | \phi_{G'} \rangle$ is the Hamiltonian matrix, $S_{G,G'} = \langle \phi_G | \phi_{G'} \rangle$ is the overlap matrix, and $\boldsymbol{c}$ is vector of the expansion coefficients c_G. The objective is to choose basis functions which are the most efficient in terms of required accuracy and computation time. Regarding accuracy one of the best methods is the full-potential linearized augmented plane wave (FLAPW) method [55–57] which is discussed next.

Plane waves, $e^{i(\boldsymbol{G}+\boldsymbol{k})\cdot\boldsymbol{r}}$ where $\boldsymbol{G}$ is a reciprocal lattice vector, are solutions to the Kohn-Sham equations in a constant potential and they are also of the Bloch form Eq. (17). Plane waves are analytically simple and the computations can be made efficient with the help of fast Fourier transforms so that they would form a convenient basis. However, the effective potential contains a strong Coulomb potential, which makes the wave functions strongly varying near the nuclei. Hence, a large number of plane waves should be used in order to describe the Kohn-Sham orbitals correctly.

In the linearized augmented plane wave method the problem of strong Coulomb potential is treated by dividing the space into two regions: atom centered spheres S and the interstitial region I, as shown in Fig. 7. In

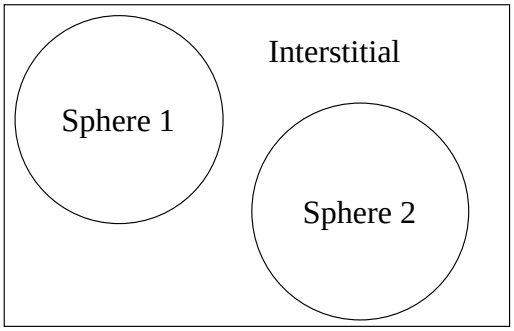

Figure 7: Division of the space into atomic spheres and into interstitial region.

the interstitial region the potential is smooth, and the plane waves can be used as a basis, while in the strong potential within the atomic spheres atomic-like orbitals are used. The basis functions can be written as

$$\phi_{\boldsymbol{k}}(\boldsymbol{G}) = \begin{cases} \frac{1}{\sqrt{\Omega}} e^{i(\boldsymbol{G}+\boldsymbol{k})\cdot\boldsymbol{r}} & \boldsymbol{r} \in I \\ \sum_{lm} [A_{lm} u_l(r) + B_{lm} \dot{u}_l(r)] Y_{lm}(\boldsymbol{r}) & \boldsymbol{r} \in S. \end{cases} \tag{20}$$

The functions $u_l(r)$ are solutions to the Schrödinger equation in the spherical potential within the atomic spheres. As such, they are energy dependent and they provide a good description of the Kohn-Sham orbitals only at the eigenenergies. Thus, a different energy parameter should be used for each state. It is possible to use $u_l(r)$ which are calculated at fixed energies e_l by adding the energy derivative $\dot{u}_l(r)$ to the basis *i.e.* linearising $u_l(r)$ around e_l. The linearized form provides a good basis for the bands in the relatively broad energy region around e_l. However, if there are states with the same orbital quantum number l but belonging to different bands (having a different principal quantum number, for instance semi-core and valence states), the linearization can result in large errors and neither of the states is described correctly. In these cases, local orbitals can be added to the basis. The local orbitals are confined to the atomic spheres and they are of the form

$$\phi_{lo} = [A_{lm} u_l(r, e_l) + B_{lm} \dot{u}_l(r, e_l)(\boldsymbol{r}) + C_{lm} u_l(r, e_l')] Y_{lm}(\boldsymbol{r}), \tag{21}$$

By choosing the other energy parameter e_l' from the semi-core energy region both semi-core and valence states are well described.

At the sphere boundary the basis functions of Eq. (20) and their derivatives are made continuous. Because of the matching condition the coefficients A_{lm} and B_{lm} depend on the reciprocal vector $\boldsymbol{G}$ and the basis functions transform like normal plane waves.

The potential, the charge and the magnetization density are expanded differently in the interstitial regions and in the atomic spheres, similarly to the Kohn-Sham orbitals. The potential, for example, is given by

$$v_{eff}(\boldsymbol{r}) = \begin{cases} \sum_S v_S \Phi_S & \boldsymbol{r} \in I \\ \sum_\nu v_\nu(r) K_\nu(\boldsymbol{r}) & \boldsymbol{r} \in S. \end{cases} \tag{22}$$

Here, symmetry-adapted basis functions are used which are the stars Φ_S in the interstitial region and the lattice harmonics K_ν in the atomic spheres. An excellent review of the details of the FLAPW method is given in [57].

Two different FLAPW implementations are used in this work. From these, the WIEN97 package [58] has been the main workhorse. Since only collinear magnetizations can be treated in this implementation, another code implementing the full density matrix formulation [59] is used for the problems where the vector magnetization density is needed.

The FLAPW method is relatively complex and the computer programs which implement the method are non-trivial. Therefore, programming errors are not unusual. Even though a semi-commercial program package WIEN97 has been used, a substantial amount of time during this work has been spent in testing and debugging of the computer codes.

4 Results

4.1 Candidates for MSM alloys

The MSM effect requires the existence of a martensitic transformation in a magnetic material. Following this aspect, some alloys are suggested as candidates in Publication I. The choice of candidate materials is guided by the known properties of the existing MSM alloy Ni_2MnGa. The studied materials are similar Heusler alloys of type X_2YZ shown in Table 4.1 where three groups of materials are separated. The X and Y components are chosen from the transition metals and Z is from the third or the fourth group of the periodic table. In the first group in Table 4.1 the X element is different from Ni_2MnGa and the second group varies the Z component. In the third group both X and Y are varied.

As a first step, the magnetic moments and the theoretical lattice constants for the assumed $L2_1$ austenite structure are calculated. The theoretical results are in agreement with the experiments in the cases where experimental data exist, as shown in Table 4.1. For the alloys containing Mn most of the magnetic moment originates from Mn. The magnetic moment originating from Ni is relatively small and the Z element shows a tiny antiferromagnetic contribution in all cases. The highest magnetic moment is in Fe_2CoGa which makes it a good candidate at this stage.

Even though the martensitic phases appear at finite temperatures, the martensitic structures should appear at least as local minima in the total energy surface at zero temperature. Therefore, the possibility of the martensitic transformations can be studied by calculating the total energy for various structures. Based on the experimental results for Ni-Mn-Ga the chosen structures are volume-conserving tetragonal and orthorhombic deformations of the cubic $L2_1$ structure. The shuffling of the atomic planes is not included here.

None of the studied materials show energy minima with orthorhombic structures, but there are some minima with tetragonal deformations. The total energies as a function of the tetragonal distortion are shown in Fig. 8 where the tetragonality is measured as the ratio of the c and a lattice constants. The compounds Ni_2MnAl, Ni_2MnGa, Ni_2CoGa, and Fe_2CoGa posses tetragonal minima. The cubic structures in Ni_2CoGa and Fe_2CoGa are unstable with large energy differences between the tetragonal minima. Therefore,

Table 1: Studied materials, their cubic lattice constants a and the magnetic moments per formula unit μ_{total} and per atom μ_i. Experimental values are shown in parenthesis.

X_2YZ	a (a.u.)	μ_{total} (μ_B)	$\mu_i(\mu_B)$
Co_2MnGa	10.82	4.08	0.76 (Co)
	(10.90[a])	(4.05[a])	2.72 (Mn)
			-0.07 (Ga)
Ni_2MnAl	10.95	4.03	0.38 (Ni)
	(11.01[a])	(4.19[b])	3.30 (Mn)
			-0.06 (Al)
Ni_2MnGa	10.98	4.09	0.37 (Ni)
	(11.01[a])	(4.17)	3.36 (Mn)
			-0.04 (Ga)
Ni_2MnSn	11.45	4.08	0.24 (Ni)
	(11.44[a])	(4.05)	3.53 (Mn)
			-0.03 (Sn)
Ni_2CoGa	10.81	1.78	0.16 (Ni)
			1.55 (Co)
			-0.02 (Ga)
Fe_2CoGa	10.92	6.05	2.20 (Fe)
			1.83 (Co)
			-0.07 (Ga)

[a] Ref. [19]
[b] Ref. [60]

these materials cannot be suggested as realistic candidates. In Ni_2MnAl the energy of the tetragonal structure is 0.6 mRy higher than for the cubic structure. Hence, the martensitic structure cannot appear as a low-temperature phase, but as the energy difference is small it is possible that a change in composition can alter the situation.

In the case of Ni_2MnGa there is a global energy minimum at tetragonal structure with $c/a \sim 1.25$, implying that it is the most stable structure at low temperatures. At the time of Publication I this structure was observed experimentally in a few cases with an applied stress [13, 61]. However, later experiments [21, 22, 28] have confirmed our theoretical prediction: even

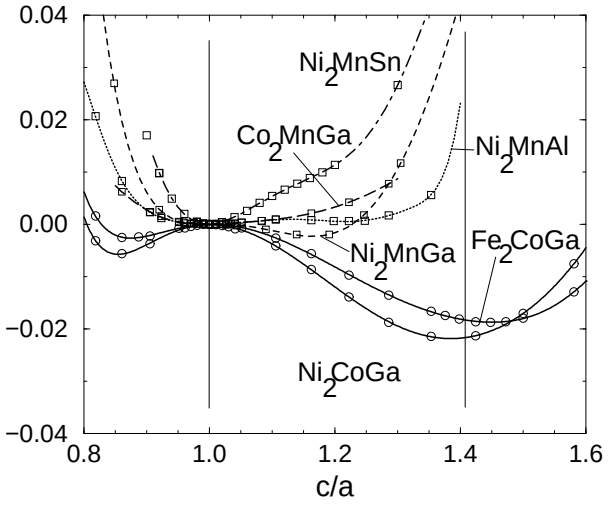

Figure 8: Total energies as a function of the tetragonal distortion for various alloys.

without external stress the tetragonal structure with $c/a \sim 1.25$ appears at low temperatures.

4.2 Stabilization of tetragonal phases

Based on some later experiments [31] and developments in the computational methods, the tetragonal deformations in Ni_2MnGa are studied with a higher accuracy in Publication II. As seen in Fig. 9, an energy minimum, albeit small, appears at $c/a = 0.94$. Therefore the modulation of the atomic planes which was earlier blaimed for the absence of this minimum is not necessary for its occurrence.

Based on the results of Publications I and II the appearance of the tetragonal structures can be ascribed to a band Jahn-Teller effect in the Ni spin down bands. In Ni_2Mn(Al,Ga,Sn) the density of states near the Fermi-level originates mainly from the spin down d_{e_g}-electrons of Ni. In the tetragonal symmetry these doubly degenerate states are split into d_{z^2}- and $d_{x^2+y^2}$-states. With a certain tetragonal distortion the splitting of the bands can cross the Fermi-level lowering the band energy. If the d_{e_g}-states in the cubic structure are close enough to the Fermi-level the reduction of the band energy can decrease the total energy. This explanation is linked with the dif-

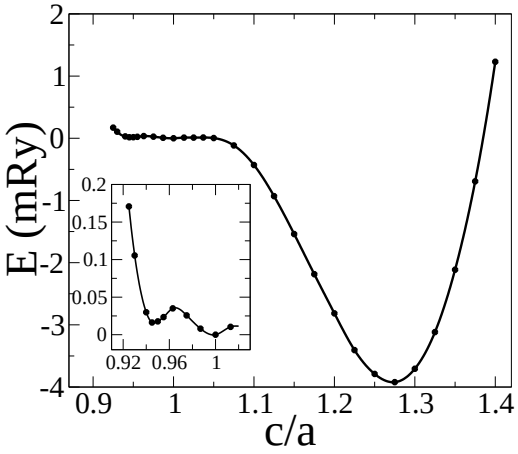

Figure 9: Total energy of Ni_2MnGa as a function of the tetragonal distortion.

ferent behaviour in Ni_2MnAl, Ni_2MnGa, and Ni_2MnSn, where the d_{e_g}-states are at different positions with respect to the Fermi-level.

The band Jahn-Teller effect results also in the redistribution of magnetization in the cubic to tetragonal transformation, which has been studied experimentally with polarized neutron scattering [31]. The theoretical results obtained in Publication II are shown in Fig. 10. The redistribution of the magnetization densities near Ni sites is similar in the theory and experiments which confirms the band Jahn-Teller picture. The experiments had reported that redistribution is caused by an increase in the number of the d_{z^2}-electrons. However, the experimental interpretation of the orbital characters of the split Ni states is based on *a priori* assumptions. Therefore, the theoretical calculations offer a refined interpretation without any extra assumptions. The magnetization difference which is elongated in the z-direction near Ni points to a change in the occupation between the d_{z^2}- and $d_{x^2+y^2}$-orbitals. The positive value of the redistribution implies a decrease in the number of the minority d_{z^2}-electrons and an increase in the occupied $d_{x^2+y^2}$ states. This behaviour is seen also in the density of states and it is opposite to the earlier experimental interpretation.

4.2.1 Elastic constants

Elastic constants are basic material parameters which describe how the material responds to external stresses. In the linear theory of elasticity the

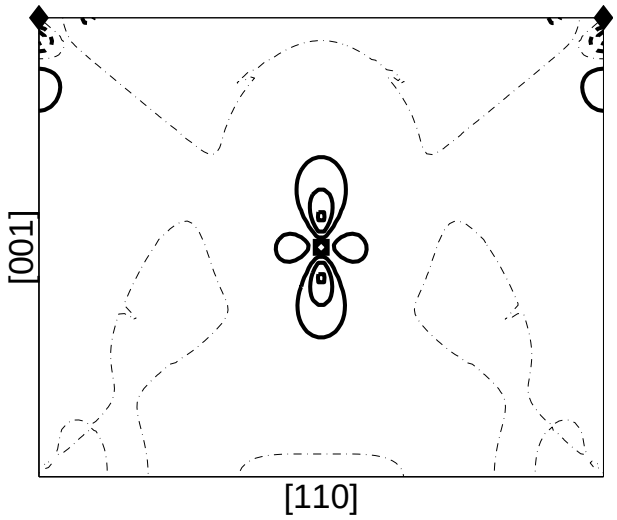

Figure 10: Redistribution of magnetization which occurs due to the transformation from the cubic structure to the tetragonal structure with $c/a < 1$. The plot shows the section parallel to [110] passing through the origin. The contours intervals are at 0.125 μ_B Å^{-3}; negative contours are shown as dashed lines. The dot-dashed lines show the zero contour level.

elastic constants relate the energy density U and the strain tensor e_j as

$$U = \frac{1}{2} \sum_{i,j=1}^{6} C_{ij} e_i e_j, \tag{23}$$

where C_{ij} are the elastic constants and the Voigt notation for the indices is used [48, 62]. The elastic constants can therefore be determined by calculating the total energy as a function of different strains. Next, some strains which are convenient for the evaluation of the elastic constants are given.

In the cubic symmetry there are only three independent elastic constants, and the following deformations characterize completely the elastic properties of a cubic crystal. A volume-conserving tetragonal deformation can be written in matrix form as

$$\begin{bmatrix} x_1' \\ x_2' \\ x_3' \end{bmatrix} = \begin{bmatrix} 1+\delta & 0 & 0 \\ 0 & 1+\delta & 0 \\ 0 & 0 & \frac{1}{(1+\delta)^2} \end{bmatrix} \begin{bmatrix} x_1 \\ x_2 \\ x_3 \end{bmatrix}. \tag{24}$$

The energy density U depends on this distortion as

$$U = 6C'\delta^2 + O(\delta^3), \tag{25}$$

where we have defined the tetragonal elastic constant C'. Similarly, a volume-conserving orthorhombic deformation is given by

$$\begin{bmatrix} x_1' \\ x_2' \\ x_3' \end{bmatrix} = \begin{bmatrix} 1 & \delta & 0 \\ \delta & 1 & 0 \\ 0 & 0 & \frac{1}{1-\delta^2} \end{bmatrix} \begin{bmatrix} x_1 \\ x_2 \\ x_3 \end{bmatrix} \tag{26}$$

and the energy density becomes

$$U = 2G\delta^2 + O(\delta^4) \tag{27}$$

with the shear constant G. Furthermore, the bulk modulus B is related to the uniform deformation as

$$U = \frac{1}{2}B\delta^2, \tag{28}$$

where δ is the relative change in the volume $\delta = \Delta V/V$.

The cubic elastic constants which appear in Eq. (23) are C_{11}, C_{12} and C_{44}, and they can be determined from the relations $G = C_{44}$, $C' = (C_{11} - C_{12})/2$ and $B = (C_{11} + 2C_{12})/3$. In other symmetries there are more independent elastic constants and C',G and B are combinations of them. In the tetragonal symmetry, for instance, there are 6 elastic constants.

The elastic constants B, C' and G of Ni_2MnGa obtained from the calculated total energies are presented in Table 2. The bulk modulus B varies slightly in the different structures while the other constants show stronger variation. The small value of C' in the cubic structure indicates softness of the lattice. Also, it can be noted that the elastic anisotropy factor G/C' ($G/C' = 1$ for an elastically isotropic material) is large in all cases, especially in the cubic structure.

4.2.2 Finite temperature effects on stability

As the density-functional theory is a ground state theory, all the previous quantities obtained directly from the calculations refer to zero temperature. However, based on the calculated results, it is possible to estimate some finite temperature properties. Here, the theoretical elastic constants are used in order to determine the effects of lattice vibrations in the stability of the martensitic phases in Ni_2MnGa at elevated temperatures.

Table 2: Elastic constants of Ni_2MnGa in the different phases. Experimental values are in parentheses.

	B (GPa)	C' (GPa)	G (GPa)
Cubic	156	4.2 (4.5[a])	120
c/a=0.94	158	12 (7.6[b])	133
c/a=1.27	161	30	66

[a] Ref. [63]
[b] Ref. [64]

At a finite temperature T the equilibrium phase is determined by the minimum of the free energy

$$F(T) = U(T) - TS(T), \tag{29}$$

where U and S are the internal energy and entropy. In an ideal defect-free system one can separate three kind of contributions in the free energy: the electronic excitations, the lattice vibrations and the magnetic excitations. Here, the main focus is in the lattice vibrations but the electronic contribution is also included since it is directly available from the calculations.

The electronic contribution is calculated by weighting the one electron eigenvalues with the Fermi-Dirac distribution

$$F_{ele} = \sum_i f_i e_i - k_B \sum_i [f_i \ln(f_i) + (1 - f_i) \ln(1 - f_i)], \tag{30}$$

where the first term gives the internal energy and the second term the electronic entropy [48]. Summations are over the occupied states in the first Brillouin zone, k_B is the Boltzmann constant and $f_i = \left(e^{(e_i - e_F)/k_B T} + 1\right)^{-1}$ is the Fermi-Dirac distribution function.

In the quantum theory of a harmonic crystal the lattice vibrations are quantized as phonons having energies

$$e_{ph} = (1/2 + n)\omega, \tag{31}$$

where the occupation number n can have integer values from zero to infinity [48]. In a crystal with N unit cells and p atoms per cell there are $3pN$ degrees of freedom for the lattice vibrations and the phonon frequencies

can be characterized with $3p$ branches each having N values within the Brillouin zone $\omega = \omega_s(\boldsymbol{q})$. Three of these branches are acoustic having a zero frequency at $q = 0$ and the remaining 3(p-1) branches are optic. The partition function for the phonons is

$$Z = \sum_{\boldsymbol{q},s} \sum_{n} e^{-\beta(1/2+n)\omega_s(\boldsymbol{q})}, \tag{32}$$

where the first summation is over the Brillouin zone and the different branches s, and the second summation is over all the possible occupation numbers. The vibrational free energy is obtained from the partition function as $F = -k_B T ln(Z)$ which gives

$$F_{vib} = \sum_{\boldsymbol{q},s} \omega_s(\boldsymbol{q})/2 + k_B T \sum_{\boldsymbol{q},s} ln\left(1 - e^{\beta\omega_s(\boldsymbol{q})}\right). \tag{33}$$

The first term is the zero-point energy *i.e.* due to the uncertainty principle there are lattice vibrations even at zero temperature. The calculation of the vibrational energy from Eq. (33) is straightforward after the phonon dispersion $\omega_s(\boldsymbol{q})$ is known. Even though the phonon dispersion curves can be calculated from first-principles [65] the computational task is demanding. Therefore the real phonon dispersion is approached here by the Debye model [66].

In the Debye approximation the continuum limit is taken, where the dispersion of ω is linear in q

$$\omega(\boldsymbol{q}) = cq, \tag{34}$$

with the speed of sound c. The linear dispersion Eq. (34) corresponds to the acoustic branches and difference between them can be included by observing that there are three independent sound velocities. The optical branches are neglected. The discrete nature of the actual lattice limits the maximum q, which can be taken into account by a cut-off frequency $\omega_D^3 = 6\pi^2 c_m^3/V$. Here, V is the volume of the unit cell and c_m is the mean sound velocity. Furthermore, by introducing the Debye temperature $\theta_D = \omega_D/k_B$ the free energy of Eq. (33) is evaluated as

$$F_{vib} = -k_b T[D(\theta_D/T) + 3\ln\left(1 - e^{\frac{-\theta_D}{T}}\right) - \frac{9\theta_D}{8T}], \tag{35}$$

where $D(x)$ is the Debye function. At this stage the only unknown quantity is the mean sound velocity c_m, which is related to the elastic constants and

can be determined from them [67]. Therefore, it is possible to estimate the vibrational free energy within the Debye model in an *ab initio* manner by using Eq. (35) together with the calculated elastic constants.

In Publication III the above procedure is used in order to calculate the free energy $F = F_{ele} + F_{vib}$ for the cubic structure and for the two theoretical tetragonal structures. The Debye temperatures are determined from the elastic constants B, C' and G. The obtained free energies are shown in Fig. 11 as a function of the temperature.

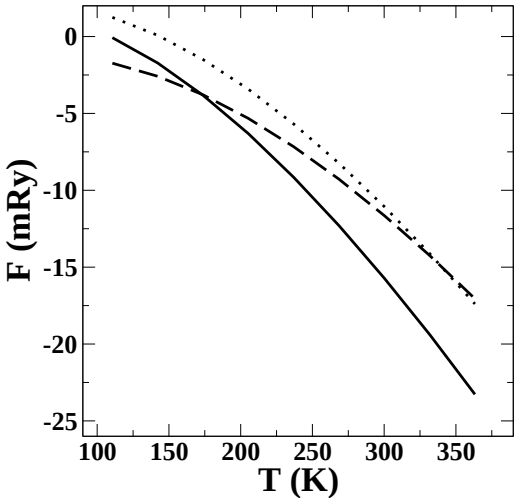

Figure 11: Free energy as a function of the temperature. Solid line: cubic; dashed line: $c/a = 1.27$; dotted line: $c/a = 0.94$.

At low temperatures the structure with $c/a = 1.27$ has the lowest free energy, while the cubic structure is the most stable at high temperatures, in accordance with the experiments. The transition temperature 200 K is in agreement with the experimental values which range from 200 K to over 600 K [15]. As the most important contribution to the free energy comes from the vibrational entropy, it can be concluded that the transition from the cubic structure to the tetragonal structure with $c/a = 1.27$ is driven by the vibrational entropy. The tetragonal structure with $c/a = 0.94$ is not stable at any temperature within the model. However, this structure has lower free energy than the structure with $c/a = 1.27$ above 350 K. Experimentally, there is strong temperature variation in the elastic constant C' of the cubic structure which is associated with a softening of some phonon branches [14, 68]. The phonon softening is beyond the linear dispersion

of the Debye model, but if its effects would be included, the tetragonal structure with $c/a = 0.94$ could be stabilized in some temperature range.

4.3 Magnetic anisotropy energy

As described in Sec. 1.1 the magnetic anisotropy energy (MAE) is the driving force in the MSM effect and it is therefore one of the most important material properties of Ni_2MnGa. As the MSM effect takes place in the martensitic phase the magnetic anisotropy energy is calculated in both tetragonal structures and in the orthorhombic structure of Ni_2MnGa. The two basic origins of the magnetic anisotropy energy are the magnetic dipole-dipole interaction which is affected by the sample shape and the relativistic spin-orbit coupling (Eq. (13)). Generally, the dipole-dipole energy is small in bulk systems and most of the anisotropy is due to the spin-orbit term.

As the spin-orbit coupling is small in transition metals its effect can be calculated in a perturbative way. According to the so-called force theorem [69, 70] the energy changes caused by small perturbations can be calculated as a difference in the eigenvalue sums,

$$\Delta E = \sum_i e_i - \sum_i e'_i \tag{36}$$

where e_i are the eigenvalues with the non-perturbed Hamiltonian, e'_i the perturbed eigenvalues, and the summation is over the occupied electronic states and the Brillouin zone. The important point is that e'_i are calculated *non-self-consistently* in a single iteration step starting from the non-perturbed density. In the presence of magnetization the spin-orbit coupling can lower the symmetry of the system as described in the Appendix. Within the force theorem the self-consistent calculation can be done with the full symmetry allowed by the crystal, and only the perturbed eigenvalues have to be calculated in the larger irreducible Brillouin zone. Also, the MAE is a small quantity (typically $\sim$1 μeV in cubic transition metals and $\sim$100 μeV in lower symmetry) so that the subtraction of band energies of the order of 1 eV is numerically more stable than the subtraction of total energies of the order of 1000 eV.

Because of the smallness of the magnetic anisotropy energy, the Brillouin zone integrations have to be done carefully with a large number of $\boldsymbol{k}$-points. The actual integration method is also important. Because the magnetic

anisotropy is sensitive to the band structure near the Fermi-level only small broadening widths can be used when averaging over the Fermi-energy. On the other hand, the tetrahedron method does not have extra parameters. Since its convergence is at least as good as with broadening schemes, it should be the method of choice in the context of MAE.

The tetragonal phases of Ni_2MnGa are assumed to be magnetically uniaxial. In such a case the symmetry forces the total energy to depend on the magnetization direction as [71]

$$E = K_1 \sin^2(\theta) + K_2 \sin^4(\theta) + ..., \tag{37}$$

where K_1 and K_2 are the first and second anisotropy constants and θ is the angle between the magnetization and the z-axis. The magnetic anisotropy energy is defined as the energy difference $E(\pi/2) - E(0) = K_1 + K_2$. The second-order term K_1 is typically larger than the fourth-order term K_2. In Publication III the angular dependence of the total energy is calculated in the tetragonal structure with $c/a = 0.94$. The results presented in Fig. 12 show that the c-axis is the easy axis and the MAE is 180 μeV[1]. A fit to

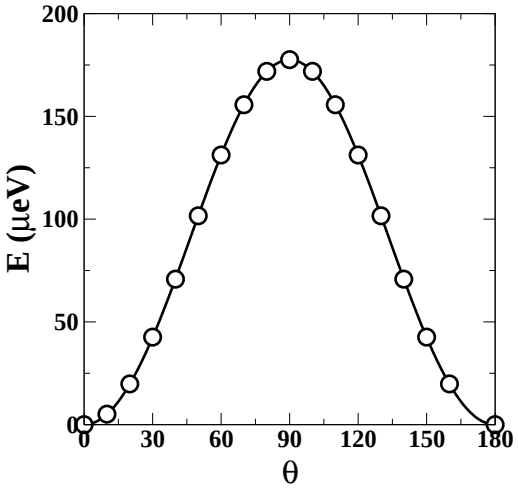

Figure 12: Total energy as a function of the magnetization direction θ. Solid line is a fit to Eq. (37).

Eq. (37) gives the anisotropy constants $K_1 = 179$ μeV and $K_2 = 1$ μeV, so that the angular dependence of the energy is characterized completely

[1]The energy units are generally Ry throughout this thesis. However MAE is given in eV as it is used traditionally in other works

by K_1. Therefore this tetragonal structure can be considered as an ideal uniaxial system.

However, there can be several twins in the martensitic phase which may complicate the interpretation of the experiments. The effect of twinning is estimated by calculating the average over two twins whose easy axes are perpendicular to each other

$$\begin{aligned} E_{ave} &= K_1 \sin^2(\theta) + K_2 \sin^4(\theta) \\ &\quad + K_1 \sin^2(\theta + \pi/2) + K_2 \sin^4(\theta + \pi/2) \\ &= K_1 + K_2(1 - 2\sin^2(\theta) + 2\sin^4(\theta)). \end{aligned} \tag{38}$$

According to the above equation the angular contribution of K_1 may average out and only the K_2 contribution is measured when several twins are present. The K_2 constant appears in both the second order and the fourth order terms but with opposite signs. The puzzling experiments in Ref. [72] report values of $K_1 = -1.3$ μeV and $K_2 = 1.1$ μeV which according to our interpretation points clearly to an average over different twins.

Next, the ordinary magnetostriction of Ni_2MnGa is estimated. According to the linear magnetoelastic theory the total energy can be written as a sum of magnetoelastic and elastic energy [73]

$$E_{tot} = -\alpha B\epsilon + C\epsilon^2, \tag{39}$$

where ϵ is the tetragonal distortion, $\epsilon = 2/3(c/a-1)$, $\alpha = 1$ for the magnetization parallel to tetragonal [001] axis and $\alpha = -1/2$ for the magnetization perpendicular to that axis. B is the magnetoelastic coupling constant which is related to the magnetic anisotropy energy and C is related to the elastic constant C', $C = 3V_0C'/2$ where V_0 is the volume of the unit cell. The magnetostriction coefficient λ_{001} is defined as the strain that minimizes the total energy of Eq. (39):

$$\lambda_{001} = -\frac{B}{2C}. \tag{40}$$

Calculations of the magnetic anisotropy energy as a function of tetragonal distortion in Publication IV show that with small distortions the variation of MAE is linear and the linear magnetoelastic theory is valid. The magnetostriction coefficient is estimated to be of the order of 10^{-2} %. This is such a small value that ordinary magnetostriction is a minor effect compared to the actual MSM effect of the order of 10 %.

In Publication IV the microscopic origins of the magnetic anisotropy energy are analyzed in terms of the orbital moment anisotropy. The orbital magnetic moment is also due to the spin-orbit coupling and there is a close relationship between the orbital moment anisotropy and the magnetic anisotropy energy [74–76]. Within second order perturbation theory the magnetic anisotropy energy can be written as

$$\Delta E_{aniso} = \frac{\xi_{\mathrm{Ni}}}{4}\Delta\mu_{\mathrm{Ni}} + \frac{\xi_{\mathrm{Mn}}}{4}\Delta\mu_{\mathrm{Mn}}, \tag{41}$$

where ξ_q and $\Delta\mu_q$ are the spin-orbit coupling strength and the orbital moment anisotropy, respectively. The role of the constituent atoms in the overall magnetic anisotropy energy can be analyzed with the help of Eq. (41). The calculated orbital moment anisotropies and magnetic anisotropy ener-

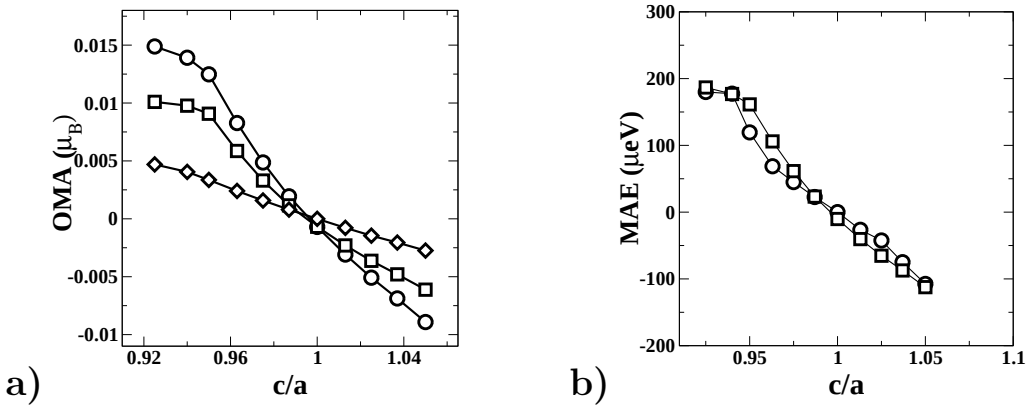

Figure 13: a) Orbital moment anisotropies as a function of the tetragonal distortion. ◯ total, □ Ni, and ◊ Mn. b) Magnetic anisotropy energy calculated with ◯ force theorem; with □ Eq. (41).

gies are shown in Fig. 13. The MAE which is calculated from Eq. (41) with spin-orbit coupling strengths $\xi_{\mathrm{Ni}} = 60$ meV and $\xi_{\mathrm{Mn}} = 30$ meV fits well to the one obtained from the eigenvalues. The results show that in Ni_2MnGa the most important component with respect to the magnetic anisotropy energy is Ni in contrast to the magnetic moment which is given mainly by Mn.

The magnetic anisotropy energy is studied also in the tetragonal structure with $c/a = 1.27$ and in the orthorhombic structure. In this tetragonal structure the c-axis is the hard axis and there is an easy plane with 300 μeV lower energy. There are three inequivalent crystal axes in the orthorhombic

structure, and the total energy is calculated when the magnetization is aligned with these axes. It appears that the MAE depends on the lengths of the orthorhombic crystal axes. The shortest axis is the easy axis, while the longest axis is the hard axis, the third one being between these two both in length and energy. The energy difference between the easy and the hard axis is 150 μeV, and between the easy and the "mid-easy" axis the MAE is 110 μeV. This finding, that in Ni_2MnGa the easy magnetization direction is always along the shortest crystal axis, has been later confirmed experimentally [4, 21, 34].

4.4 Estimation of the Curie temperature

A ferromagnetic material loses its long range magnetic order and becomes paramagnetic at the Curie temperature. This temperature is therefore one of the key parameters determining the operation range of the MSM effect. From a more fundamental point of view the Curie temperature is a basic property for the theoretical understanding of a ferromagnetic material. The decrease of macroscopic magnetization with increasing temperature is caused by longitudinal and transverse fluctuations of magnetic moments. It is assumed that transverse excitations of magnetization are the dominant origin for the Curie temperature in transition metals because large local magnetic moments are shown to exist above the Curie point [77, 78]. These transverse excitations are quantized as magnons.

In Publication V the magnon related properties of Ni_2MnGa and Ni_2MnAl are studied with total-energy calculations of spin spirals. The spin spiral is a magnetic configuration where the magnetization direction varies with a well-defined period. The period is determined by the wave vector $\boldsymbol{q}$ as

$$\boldsymbol{M}(\boldsymbol{r}_n) = m_n \begin{pmatrix} \cos(\boldsymbol{q}\cdot\boldsymbol{r}_n + \phi_n)\sin(\theta_n) \\ \sin(\boldsymbol{q}\cdot\boldsymbol{r}_n + \phi_n)\sin(\theta_n) \\ \cos(\theta_n) \end{pmatrix}, \tag{42}$$

where polar coordinates are used and m_n is the magnetic moment of atom n with a phase ϕ_n at the position $\boldsymbol{r}_n$. A more general definition of the spin spiral is given by

$$\boldsymbol{M}(\boldsymbol{r}+\boldsymbol{R}) = D(\boldsymbol{q}\cdot\boldsymbol{R})\boldsymbol{M}(\boldsymbol{r}), \tag{43}$$

where R is a lattice translation and D is a rotation around the z-axis. This definition allows the magnetization to vary freely within the unit cell. An example of a spin spiral in the $L2_1$ structure is shown in Fig. 14.

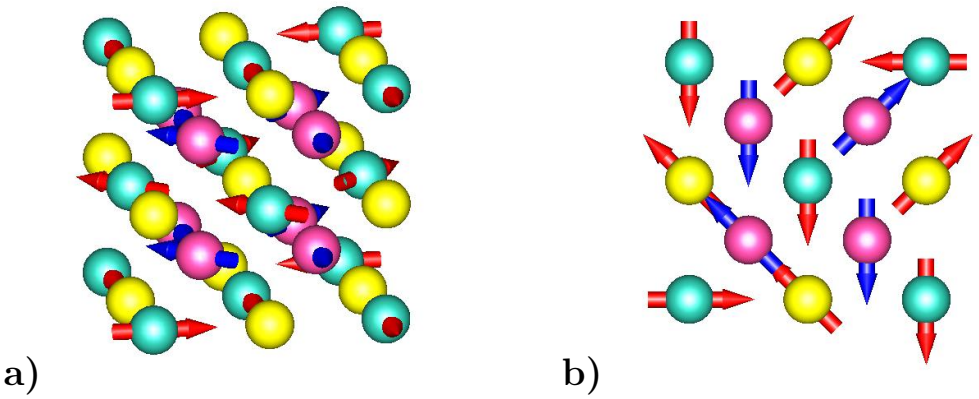

Figure 14: Spiral magnetic configuration where $\theta = \frac{\pi}{2}$, $\phi = 0$ and $\boldsymbol{q} = (\frac{2}{3}\ \frac{2}{3}\ 0)\frac{2\pi}{a}$ in the $L2_1$ structure. a) Full view, b) top view.

As a spin spiral is inherently a non-collinear magnetic configuration the full density matrix formulation of the density-functional theory has to be used (see Sec. 3). The spiral magnetic configuration breaks the translational symmetry of the crystal so at first sight it seems that one should use large supercells. However, as shown in the Appendix, the chemical unit cell can be used by defining generalized translations which consist of translations in real space and rotations in spin space.

The total energy as a function of the spiral vector $\boldsymbol{q}$ is shown in Fig. 15 for the high symmetry directions [001], [111] and [110]. It is seen that the energies are very similar both in Ni_2MnGa and in Ni_2MnAl. For small values of q the energy grows quadratically, but the dispersion flattens for larger q especially in the [110] direction.

A spin spiral describes a spatially rotating magnetization and it can be therefore correlated with a frozen magnon. The magnon energy is obtained from the total energy of the planar ($\theta = \pi/2$) spiral as [79, 80]

$$\omega_q = \frac{4\mu_B}{M} E(\boldsymbol{q}), \tag{44}$$

where M is the magnetic moment per unit cell. In the long wavelength limit where the magnon dispersion is quadratic, the spin stiffness constant D can be defined as

$$\omega_q = Dq^2. \tag{45}$$

The theoretical spin stiffness obtained from the total energies shown in

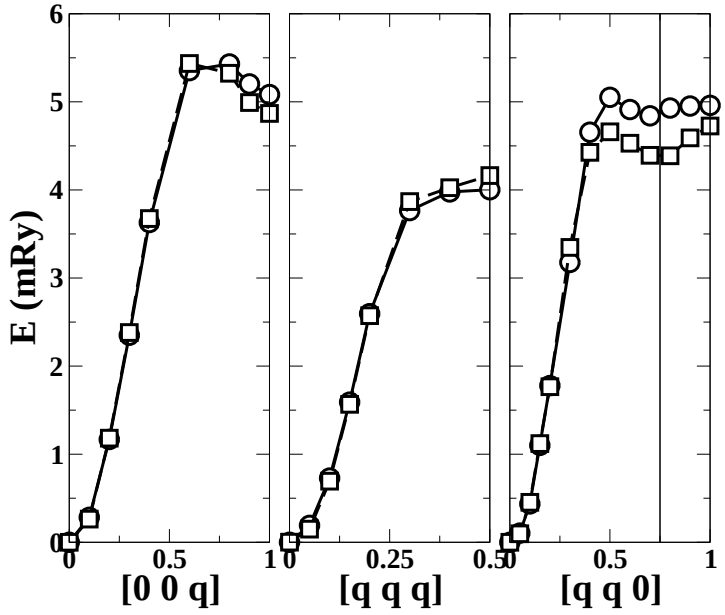

Figure 15: Total energy as a function of the spiral vector $\boldsymbol{q}$ in the units of 2π/a. ◯ Ni_2MnAl, □ Ni_2MnGa.

Fig. 15 is $D = 77$ mRy a.u.^{2} and it is in good agreement with the experimental value of 79 mRy a.u.^{2} measured in Ni-Mn-Ga films [81].

The Curie temperature can be estimated from the calculated energy dispersions in Fig. 15. In contrast to the phonons, magnons can be considered as non-interacting bosons only at low temperatures. Therefore some extra assumptions have to be made when determining the Curie temperature. Within the random phase approximation the Curie temperature T_C is given by [82, 83]

$$\frac{1}{k_B T_C} = \frac{6\mu_B}{M} \frac{V}{(2\pi)^3} \int d^3q \frac{1}{\omega_q}, \tag{46}$$

where V is the unit cell volume, and the integration is over the Brillouin zone. The determination of T_C from Eq. (46) requires knowledge of the magnon spectra in the whole Brillouin zone. We have simplified the problem by working in the spirit of the Debye approximation for the phonons. The Brillouin zone is replaced with a sphere and the dispersion is considered quadratic up to some radius q_c and constant thereafter (see Fig. 15). With

these approximations the Curie temperature is given by

$$\frac{1}{k_B T_C} = \frac{V}{M\pi^2}\left(\frac{3q_c}{D} + \frac{q_d^3 - q_c^3}{\omega_c}\right), \tag{47}$$

where $q_d = (6\pi^2/V)^{1/3}$ and ω_c is the constant energy. Using the calculated spin stiffness and ω_c=5 mRy when $q > 0.7q_D$, we obtain the Curie temperature 480 K. This value is in good agreement with the experimental one 380 K. As the energy dispersions in Fig. 15 are similar for Ni_2MnGa and Ni_2MnAl this estimate of Curie temperature applies for both materials.

More insight into the energy dispersion and to the Curie temperature is obtained by studying the behaviour of magnetization with the spiral vector $\boldsymbol{q}$. The analysis shows that the magnetic moment of Mn remains practically constant while the Ni moment varies considerably. It is found that a large magnetization near the Ni sites is correlated with a decrease in the energy. This suggests that the Curie temperature could be increased by reducing the magnetic moment at the Ni site, for example by alloying with non-magnetic elements such as Cu. More details about this issue can be found in Publication V.

4.5 Alloying effects

Up to now, all results have been obtained for ideal stoichiometric compounds. The previous calculations give information about the role of the constituent atoms in determining the material properties. However, the conclusions do not necessarily apply for all the effects when alloying with these constituents. Thus, calculations of non-stoichiometric compositions are needed. Here, two different methods are used to study these alloying effects.

4.5.1 Rigid band approximation

The rigid band approximation is the simplest approach for estimating alloying effects. It can be shown [84] that when hybridization between the states with different angular momentum character (s,p,d-orbitals) is neglected and the potential is spherically symmetric the Hamiltonian can be separated into two contributions. One part is the structure factor which depends only on

the geometry of the crystal lattice, and the other term is the potential function which depends on the potential within the atomic spheres. If the potential function is assumed to be constant, the band structure depends only on the crystal structure. Within this picture, the elements in the $3d$-series differ only on the number of electrons which determines the Fermi-level. This canonical band model is at the heart of the rigid band approximation. The band structure is calculated for the stoichiometric compound, while the non-stoichiometry is designated through the number of valence electrons by adjusting the Fermi-level.

The variation of the magnetic moments with band filling is shown in Fig. 16a. The magnetic moment of Mn remains constant for a wide range of electron concentrations because there are only few Mn states near the Fermi-level. In contrast, there are several Ni states around the Fermi-level and the Ni moment shows a linear variation of the magnetic moment with the band filling. However, according to experiments reported in Publication VI the total magnetic moment *decreases* when the electron concentration is lower than the stoichiometric one. Also, the decrease of the magnetic moment is too small to explain the experimental trend with larger electron concentrations.

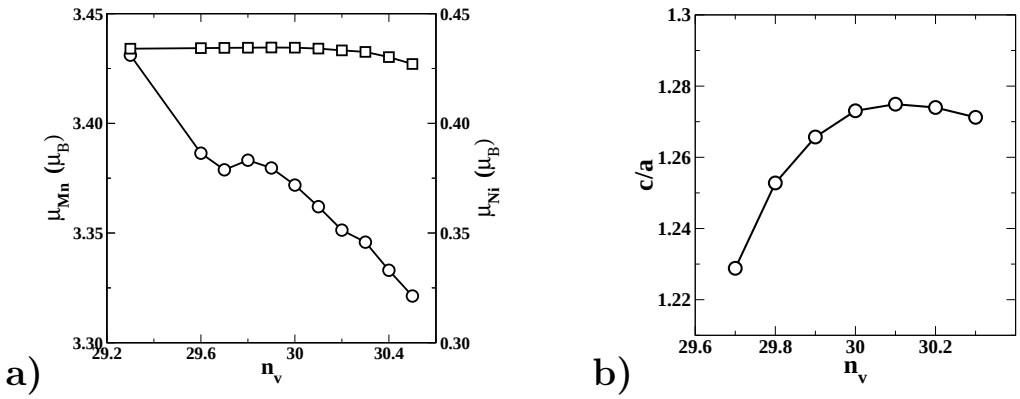

Figure 16: a) Magnetic moments of Mn □ and Ni ◯ and b) tetragonality as a function of the number of valence electrons n_v. The stoichiometric composition corresponds to $n_v = 30$.

In Publication III the rigid band approximation is used to study the effect of alloying for the appearance of tetragonal energy minima. The optimum c/a ratios as well as the energy differences between minima vary with electron concentration. The variation of the equilibrium c/a ratio with electron concentration in the phase with $c/a \sim 1.2$ is shown in Fig. 16b. The optimum

c/a ratio increases first with band filling and, after reaching a maximum, it starts to decrease. Similar behaviour is also seen in the experiments [26]. The energy at the minimum with $c/a \sim 0.94$ decreases when decreasing electron concentration, but this minimum disappears when the band filling is larger than at the stoichiometry. This behaviour can be explained also by the band Jahn-Teller picture presented earlier. However, the structure with $c/a \sim 0.94$ is seen experimentally also with higher electron concentrations. Therefore, it is clear that the rigid band approximation will have problems describing the stability of the phases.

The magnetic anisotropy energy is also studied as a function of the band filling in Publication IV. The calculated results for the $c/a = 0.94$ structure are shown in Fig. 17 together with some experimental values. The experi-

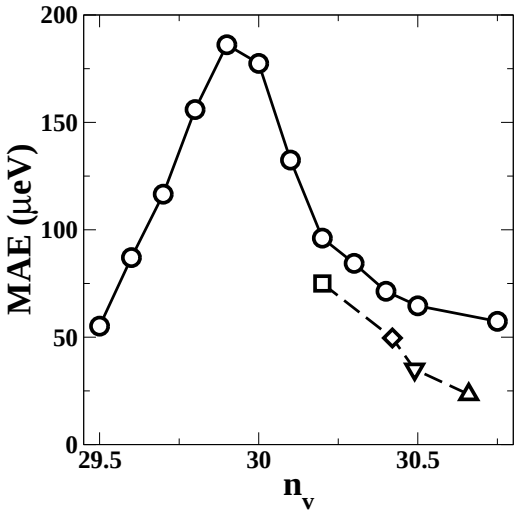

Figure 17: The MAE for $c/a = 0.94$ as a function of the number of valence electrons n_v. Experimental values from □ Ref. [32], ◊ Ref. [30], △ Ref. [85].

mental trend of decreasing MAE with increasing electron concentration is reproduced by the rigid band approximation. However, as the experimental values refer to room temperature, it is probable that the rigid band approximation actually underestimates the magnetic anisotropy energies.

4.5.2 Supercell approach

The results presented above show that, while in certain cases the rigid band approximation seems to work well, there are cases where it completely fails.

In Publication VI we have gone beyond the rigid band approximation and studied the alloying effects with supercell calculations of $Ni_2Mn_{1.25}Ga_{0.75}$.

Experimentally, compositions close to $Ni_2Mn_{1.25}Ga_{0.75}$ have good MSM properties as large strains are obtained around room temperature. This composition is obtained by replacing one Ga atom by an Mn atom in the 16-atom supercell, as shown in Fig. 18. The main difference in the supercell ap-

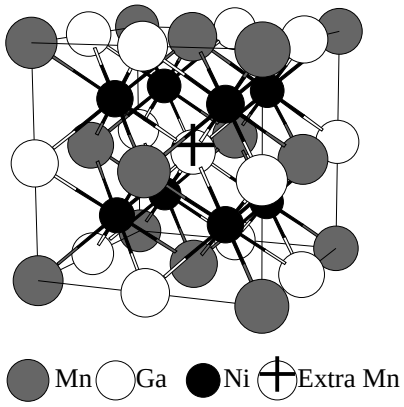

Figure 18: $L2_1$ supercell of $Ni_2Mn_{1.25}Ga_{0.75}$.

proach to the actual experimental composition is that in the supercell the extra Mn atoms are perfectly ordered while in the real material they can be distributed randomly in the Ga sites.

The most important result obtained from the calculations is that the magnetic moments of the extra Mn favor *anti-ferromagnetic* alignment with respect to the neighbouring Mn atoms. The magnetic moment of Mn is approximately a constant 3.5 μ_B regardless of the direction of the moment or electron concentration. Hence, the antiferromagnetic ordering of the extra Mn means that every additional Mn reduces the total moment by 3.5 μ_B. Hence, the magnetic moment of $Ni_2Mn_{1+x}Ga_{1-x}$ can be described with a simple model as $\mu_{total} = 2\mu_{Ni} + (1 - |x|)3.5\mu_B$ where the Ni moment μ_{Ni} is varied around the stoichiometric value 0.3 μ_B with the electron concentration according to the rigid band results. As seen in Fig. 19 the model describes well the experimental variation of the magnetization. From this agreement it can be concluded that the Mn atoms substituted at the Ga sites are antiferromagnetically coupled to the Mn atoms at Mn sites.

The extra Mn has also important consequences for the appearance of the martensitic phases. With the antiferromagnetic alignment, the structure

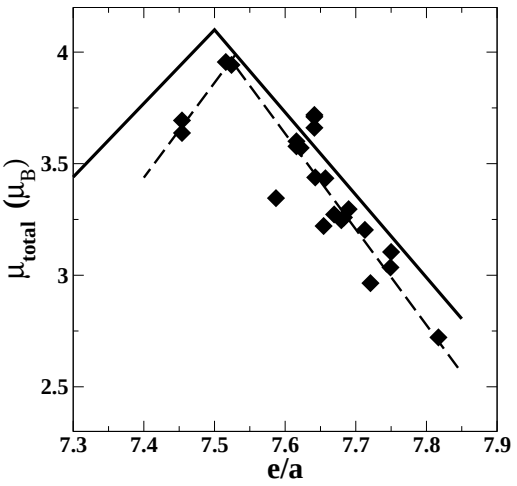

Figure 19: Saturation magnetization vs the average number of valence electrons per atom (e/a). The dashed line is a linear fit to the experimental data and the solid line is the theoretical prediction assuming a 50 % Ni content.

with $c/a = 0.94$ is stabilized and it has 5 meV lower energy per formula unit than the cubic structure. In addition, an energy minimum appears for the orthorhombic structure with lattice constant ratios $c/a \sim 0.93$ and $b/a \sim 0.97$. The energy of the orthorhombic structure is between the energies of the two tetragonal minima, so that the theoretical order of phases agrees with the experimental findings discussed in Fig. 5b of Sec. 2.

When the magnetic anisotropy energy is calculated with the extra Mn one obtains a value of 150 μeV for the ferromagnetic configuration and 100 μeV for the antiferromagnetic configuration. The corresponding rigid band value is about 50 μeV as extracted from Fig. 17. From these three values the antiferromagnetic one compares well with the low temperature experimental value of 90 μeV [34]. It can be seen that the magnetic and structural ordering is important also for the quantitative value of the magnetic anisotropy energy.

5 Conclusions

In this thesis, atomic-scale simulations for magnetic shape memory alloys are presented. The calculations are done within the density-functional theory with the state-of-the-art FLAPW-method. The main focus is on the Ni-Mn-Ga alloy which has already shown magnetic-field-induced strains of up to 10 %. Also some other materials suggested as MSM candidates are studied.

From the suggested candidate materials only Ni_2MnAl is found to have potential for the magnetic shape memory effect, but further work is needed in order to see the actual usability of this alloy. The appearance of energy minima at zero temperature as well as the different behaviour between the alloys in tetragonal deformations is ascribed to the band Jahn-Teller effect. Comparison of theoretical and experimental results with respect to the magnetization redistribution at the martensitic transformation confirms this picture. The calculated elastic constants are used to study the effect of lattice vibrations in the stability of the tetragonal phases of Ni_2MnGa. It is seen that the transition from the cubic structure to the tetragonal structure with $c/a \sim 1.27$ is driven mainly by the vibrational entropy.

The calculations of the magnetic anisotropy energy of Ni_2MnGa show that the tetragonal structure with $c/a \sim 0.94$ is magnetically uniaxial and characterized completely by the first anisotropy constant. We estimate the effect of twinning for the magnetic anisotropy: When several twins are present only the second anisotropy constant may appear in the experimental results. Also, the effect of constituent atoms to the magnetic anisotropy energy is analyzed in terms of orbital moment anisotropy. The most important constituent concerning the magnetic anisotropy is found to be Ni. The studies of magnetic anisotropy energy in the orthorhombic and in the other tetragonal structure imply that in Ni_2MnGa the shortest crystal axis is always the easy magnetization axis.

The Curie temperatures of Ni_2MnGa and Ni_2MnAl are estimated on the basis of total energy calculations of spin spirals. The Curie temperature is found to be similar in both materials. From the behaviour of magnetic moments, it is seen that Ni is important in determining the Curie temperature despite its smaller magnetic moment compared to Mn. The results suggest also that a large value of the magnetic moment at the Ni sites is correlated with a low Curie temperature.

At this step, some conclusions about the role of constituent atoms in stoichiometric Ni_2MnGa can be given. The magnetic moment originates mainly from Mn, but regarding the other properties investigated here Ni is more important. This is related to the fact that most of the electronic states near the Fermi-level are due to Ni. The Mn-states are at lower energies making Mn more inert as seen for example in the more localized character of the magnetic moment of Mn.

The alloying effects are studied with two different approaches. The simple rigid band approximation works well in many cases, reproducing the experimental trends, but it fails severely when predicting the appearance of phases at different compositions and the variation of magnetization with electron concentration. The calculations with explicit Mn-rich compositions give a more refined picture about the alloying effects. The most important consequence is that the additional Mn atoms couple antiferromagnetically to the neighbouring Mn atoms which explains the experimental composition dependence of the magnetization.

During this work many ideas for further studies have emerged. Some important problems are the calculation of the actual phonon spectra which would allow more accurate determination of the phase equilibra at finite temperatures. The studies taking into account the modulation of the tetragonal structures are already in progress as well as calculations about the twin boundary. The alloying effects should be studied in more detail. Because the supercell approach allows investigations of only few particular compositions and assumes ordering of dopant atoms, methods including disorder, like the coherent potential approximation, could provide additional information. Theoretical studies should be extended from the atomic scale also to the mesoscopic and macroscopic regimes, where the atomic scale results could be used as input. Some investigations about the twin boundary motion along this line have already been initiated.

Appendix: Symmetry and magnetism

The symmetry operations of a non-magnetic crystal are rotations and translations in space, and are classified according to the ordinary space groups. However, in a magnetic crystal there are also spin degrees of freedom which are not taken into account in the space groups. A convenient description of the symmetry properties of the magnetic crystal is given by the spin-space groups [86–88] which allow separate transformation of spin and space variables.

The spin rotations and space rotations are designated with α_s and α_r, respectively. Designating the space translations with $\boldsymbol{t}$ the operations of the spin-space group can be defined as

$$\{\alpha_s|\alpha_r|\boldsymbol{t}\}\psi(\boldsymbol{r}) = U(\alpha_s)\psi(\alpha_r^{-1}\boldsymbol{r} - \alpha_r^{-1}\boldsymbol{t}), \tag{48}$$

where U is the spin rotation matrix.

The symmetry operations of system are those operations which commute with the Hamiltonian of Eq. (14). In a non-magnetic case the Hamiltonian is a scalar times an identity matrix so that arbitrary spin rotations are symmetry operations. On the other hand, in magnetic materials the presence of a spontaneous magnetic moment restricts the possible symmetry operations. In a normal ferromagnet there is a global spin quantization axis and the allowed spin rotations are restricted to the rotations about the quantization axis. When the spin-orbit interaction is neglected, the spin space and the real space are not coupled and the magnetic moment does not affect the allowed space transformations. However, when the spin-orbit coupling is included, the spin and space parts cannot be transformed separately. The presence of magnetic moment can constrain the possible space transformations because the condition $\alpha_s = \alpha_r$ has to be fulfilled. For example, in the cubic symmetry only 16 space group operations from the 48 remain when there is a magnetization in the [001] direction.

Here, it must be noted that the magnetization is an axial vector. This means that the magnetization is invariant under spatial inversion, but changes its sign for reflections about the plane containing the magnetization. Time-inversion reverses also the magnetization direction and therefore the above reflections are symmetry operations when combined with the time inversion. In reciprocal space, time inversion is equivalent to spatial inversion, so that

real space and $\boldsymbol{k}$ space have different symmetry properties when the crystal does not have inversion symmetry.

A special case where the spin-space groups are extremely useful in the calculations is the spin spiral [89]. It was defined in Eq. (43) as

$$\boldsymbol{M}(\boldsymbol{r}+\boldsymbol{R}) = D(\boldsymbol{q}\cdot\boldsymbol{R})\boldsymbol{M}(\boldsymbol{r}). \tag{49}$$

As such, the spin spiral is not translationally invariant. However, it is possible to define generalized translations $\{\boldsymbol{q}\cdot\boldsymbol{R}|e|\boldsymbol{R}\}$ which leave the spiral invariant. These generalized translations form a group which is isomorphic to the group of ordinary translations. This leads into a generalized Bloch theorem, so that the single particle states can be characterized with a $\boldsymbol{k}$-point in the Brillouin zone and they can be written as

$$\psi_k(\boldsymbol{r}) = e^{i\boldsymbol{k}\cdot\boldsymbol{r}} \begin{pmatrix} e^{-i\boldsymbol{q}\cdot\boldsymbol{r}/2}u_k(\boldsymbol{r}) \\ e^{+i\boldsymbol{q}\cdot\boldsymbol{r}/2}d_k(\boldsymbol{r}) \end{pmatrix}. \tag{50}$$

The functions $u_k(\boldsymbol{r})$ and $d_k(\boldsymbol{r})$ are invariant with respect to lattice translations having the same role as for normal Bloch functions. With the help of the spin-space groups the chemical unit cell can be used in the calculations of spin spirals and no large supercells are needed.

Generally, the spin spiral can lower the symmetry of the system. The allowed symmetry operations can be divided into two groups. The first group contains space rotations which leave the spiral wave vector invariant

$$\alpha_r\boldsymbol{q} = \boldsymbol{q} \tag{51}$$

together with arbitrary spin rotations about the z-axis. The symmetry operations in the second group are space rotations which invert the wave vector

$$\alpha_r\boldsymbol{q} = -\boldsymbol{q} \tag{52}$$

together with spin rotations by an angle π about an axis perpendicular to the z-axis [87, 90]. In practice, the spin rotations are not necessarily implemented and one can use only the operations of type I. However, if the crystal structure is invariant under space inversion the existence of operators of type II possess symmetry constraints. For example, the magnetic moments in the planar spirals where $\boldsymbol{M} = (M_x, M_y, 0)$ have to fulfill the condition

$$(M_x(\boldsymbol{r}), M_y(\boldsymbol{r}, 0) = (M_x(-\boldsymbol{r}), -M_y(-\boldsymbol{r}, 0) \tag{53}$$

at two points related by inversion.

References

[1] R. E. Newnham, MRS Bull. **22**, 20 (1997).

[2] K. Ullakko, J. K. Huang, C. Kantner, and R. C. O'Handley, Appl. Phys. Lett. **69**, 1966 (1996).

[3] A. E. Clark, in *Ferromagnetic Materials*, edited by E. P. Wohlfarth (North Holland, Amsterdam, 1980), Vol. 1, p. 531.

[4] A. Sozinov, A. A. Likhachev, N. Lanska, and K. Ullakko, Appl. Phys. Lett. **80**, 1746 (2002).

[5] Z. Nishiyama, *Martensitic Transformation* (Academic Press, New York, 1978).

[6] D. A. Porter and K. E. Easterling, *Phase Transformations in Metals and Alloys* (Van Nostrand Reinhold, New York, 1981).

[7] *Shape Memory Alloys*, edited by H. Funakubo (Gordon and Breach Science Publishers, London, 1987).

[8] R. D. James and M. Wuttig, Philos. Mag. A **77**, 1273 (1998).

[9] M. Wuttig, J. Li, and C. Craciunescu, Scripta Mater. **44**, 2393 (2001).

[10] A. N. Lavrov, S. Komiya, and Y. Ando, Nature **418**, 385 (2002).

[11] S. J. Murray *et al.*, Appl. Phys. Lett. **77**, 886 (2000).

[12] V. V. Kokorin and M. Wuttig, J. Magn. Magn. Mater. **234**, 25 (2001).

[13] V. V. Martynov and V. V. Kokorin, J. Phys. III **2**, 739 (1992).

[14] L. Mañosa *et al.*, Phys. Rev. B **55**, 11068 (1997).

[15] J. Pons, V. A. Chernenko, R. Santamarta, and E. Cesari, Acta Mater. **48**, 3027 (2000).

[16] N. Glavatska, I. Glavatsky, G. Mogilny, and V. Gavriljuk, Appl. Phys. Lett. **80**, 3533 (2002).

[17] P. J. Webster, K. R. A. Ziebeck, S. L. Town, and M. S. Peak, Philos. Mag. B **49**, 295 (1984).

[18] A. N. Vasil'ev *et al.*, Phys. Rev. B **59**, 1113 (1999).

[19] P. J. Webster, Contemp. Phys. **10**, 559 (1969).

[20] I. K. Zasimchuk *et al.*, Phys. Met. Metall. **69**, 104 (1990).

[21] A. Sozinov, A. A. Likhachev, and K. Ullakko, Proc. SPIE **4333**, 189 (2001).

[22] W. H. Wang *et al.*, Appl. Phys. Lett. **79**, 1148 (2001).

[23] V. A. Cherneko *et al.*, Phys. Rev. B **57**, 2659 (1998).

[24] O. Heczko, N. Lanska, O. Soderberg, and K. Ullakko, J. Magn. Magn. Mater. **242-245**, 1446 (2002).

[25] G. Feng, C. Jiang, T. Liang, and H. Xu, J. Magn. Magn. Mater. **248**, 312 (2002).

[26] A. Sozinov, unpublished.

[27] V. V. Khovailo *et al.*, Phys. Rev. B **65**, 092410 (2002).

[28] C. Jiang, G. Feng, and H. Xu, Appl. Phys. Lett. **80**, 1619 (2002).

[29] A. Sozinov *et al.*, 2002, unpublished.

[30] O. Heczko, A. Sozinov, and K. Ullakko, IEEE Trans. Magn. **36**, 3266 (2000).

[31] P. J. Brown *et al.*, J. Phys.: Condens. Matter **11**, 4715 (1999).

[32] R. Tickle and R. D. James, J. Magn. Magn. Mater. **195**, 627 (1999).

[33] O. Heczko, K. Jurek, and K. Ullakko, J. Magn. Magn. Mater. **226**, 996 (2001).

[34] L. Straka and O. Heczko, to be published in J. Appl. Phys.

[35] D. R. Hartree, Proc. Cambridge Philos. Soc. **24**, 89 (1928).

[36] V. Fock, Z. Phys. **61**, 126 (1930).

[37] V. Fock, Z. Phys. **62**, 795 (1930).

[38] L. H. Thomas, Proc. Cambridge Philos. Soc. **23**, 542 (1927).

[39] E. Fermi, Z. Phys. **43**, 79 (1927).

[40] P. Hohenberg and W. Kohn, Physical Review **136**, B864 (1964).

[41] U. von Barth and L. Hedin, J. Phys. C **5**, 1629 (1972).

[42] W. Kohn and L. Sham, Physical Review **140**, A1133 (1965).

[43] M. Weissbluth, *Atoms and Molecules* (Academic Press, New York, 1978).

[44] D. D. Koelling and B. N. Harmon, J. Phys. C **10**, 3107 (1977).

[45] A. H. MacDonald, W. E. Picket, and D. D. Koelling, J. Phys. C **13**, 2675 (1980).

[46] J. Perdew *et al.*, Phys. Rev. B **46**, 6671 (1992).

[47] J. Perdew, K. Burke, and M. Ernzerhof, Phys. Rev. Lett. **77**, 3865 (1996).

[48] N. W. Ascroft and N. D. Mermin, *Solid State Physics* (Saunders College Publishing, London, 1976).

[49] H. J. Monkhorst and J. D. Pack, Phys. Rev. B **13**, 5188 (1976).

[50] M. J. Gillan, J. Phys.: Condens. Matter **1**, 689 (1989).

[51] M. Methfessel and A. T. Paxton, Phys. Rev. B **40**, 3616 (1989).

[52] O. Jepsen and O. K. Andersen, Solid State Commun. **9**, 1763 (1971).

[53] P. E. Blöchl, O. Jepsen, and O. K. Andersen, Phys. Rev. B **49**, 16223 (1994).

[54] M. Heiskanen, T. Torsti, M. J. Puska, and R. M. Nieminen, Phys. Rev. B **63**, 245106 (2001).

[55] E. Wimmer, H. Krakauer, M. Weinert, and A. J. Freeman, Phys. Rev. B **24**, 864 (1981).

[56] M. Weinert, E. Wimmer, and A. J. Freeman, Phys. Rev. B **26**, 4571 (1982), and references therein.

[57] D. Singh, *Planewaves, Pseudopotentials and the LAPW Method* (Kluwer Academic Publishers, New York, 1994).

[58] P. Blaha, K. Schwarz, and J.Luitz, *WIEN97*, Vienna University of Technology, 1997, (Improved and updated Unix version of the copyrighted WIEN-code, which was published by P. Blaha, K. Schwarz, P. Sorantin and S.B. Trickey, in Comput. Phys. Commun. 59, 399 1990).

[59] L. Nordström and D. J. Singh, Phys. Rev. Lett. **76**, 4420 (1996).

[60] K. R. A. Ziebeck and P. J. Webster, J. Phys. F **5**, 1756 (1975).

[61] V. V. Martynov, J. Physique **5**, (1995).

[62] *Mechanics of Solids and Fluids* (Springer-Verlag, New York, 1991).

[63] J. Worgull, E. Petti, and J. Trivisonno, Phys. Rev. B **54**, 15695 (1996).

[64] K. Ullakko, unpublished.

[65] S. Baroni, S. de Groncoli, A. Corso, and P. Giannozzi, Rev. Modern Phys. **74**, 515 (2001).

[66] P. P. Debye, Ann. Physik. Lpz. **39**, 789 (1912).

[67] G. A. Alers, in *Physical Acoustics*, edited by W. P. Mason (Academic Press, New York, USA, 1965), Vol. IIIB.

[68] L. Mañosa *et al.*, Phys. Rev. B **64**, 024305 (2001).

[69] A. R. Mackintosh and O. K. Andersen, in *Electrons at the Fermi Surface*, edited by M. Springford (Cambridge University Press, Cambridge, England, 1980).

[70] M. Weinert, R. E. Watson, and J. W. Davenport, Phys. Rev. B **32**, 2115 (1985).

[71] R. R. Birss, *Symmetry and Magnetism* (North-Holland publishing co., Amsterdam, 1964).

[72] B. D. Shanina *et al.*, J. Magn. Magn. Mater. **237**, 309 (2001).

[73] P. James *et al.*, Appl. Phys. Lett. **76**, 915 (2000).

[74] P. James, Ph.D. thesis, Uppsala University, 1999.

[75] P. Bruno, Phys. Rev. B **39**, 865 (1989).

[76] G. van der Laan, J. Phys.: Condens. Matter **10**, 3239 (1998).

[77] E. Kisker, K.Schröder, M. Campagna, and W. Gudat, Phys. Rev. Lett. **52**, 2285 (1984).

[78] A. Kakizaki *et al.*, Phys. Rev. Lett. **72**, 2781 (1994).

[79] N. M. Rosengaard and B. Johansson, Phys. Rev. B **55**, 14975 (1997).

[80] S. V. Halilov, H. Eschrig, A. Y. Perlov, and P. M. Oppeneer, Phys. Rev. B **58**, 293 (1998).

[81] S. I. Patil *et al.*, Appl. Phys. Lett. **81**, 1279 (2002).

[82] M. Pajda *et al.*, Phys. Rev. B **64**, 174402 (2001).

[83] C. S. Wang, R. E. Prange, and V. Korenman, Phys. Rev. B **25**, 5766 (1982).

[84] H. L. Skriver, *The LMTO Method* (Springer-Verlag, Berlin, 1984).

[85] S. Wirth, A. Leithe-Jasper, A. N. Vasil'ev, and J. M. D. Coey, J. Magn. Magn. Mater. **167**, L7 (1997).

[86] W. Brinkman and R. J. Elliott, Proc. R. Soc. A **294**, 343 (1966).

[87] L. M. Sandratskii, J. Phys.: Condens. Matter **3**, 8565 (1991).

[88] L. M. Sandratskii, Adv. Phys. **47**, 91 (1998).

[89] C. Herring, in *Magnetism*, edited by G. Rado and H. Suhl (Academic Press, New York, 1966), Vol. 4.

[90] K. Knöpfle, L. M. Sandratskii, and J. Kübler, Phys. Rev. B **62**, 5564 (2000).